

# **Methane Oxidation Activity and Nanoscale Characterization of Pd/CeO<sub>2</sub> Catalysts**

**Prepared by Dry Milling Pd Acetate and Ceria**

*Maila Danielis<sup>1</sup>, Luis E. Betancourt<sup>2</sup>, Ivan Orozco<sup>3</sup>, Núria J. Divins<sup>4</sup>, Jordi Llorca<sup>4</sup>, José A.*

*Rodríguez<sup>2,3</sup>, Sanjaya D. Senanayake<sup>2</sup>, Sara Colussi<sup>1</sup>, Alessandro Trovarelli<sup>1</sup>*

<sup>1</sup> Dipartimento Politecnico, Università di Udine, and INSTM,

via del Cottonificio 108, 33100 Udine, Italy

<sup>2</sup> Chemistry Division, Brookhaven National Laboratory, Upton, NY 11973, USA

<sup>3</sup> Chemistry Department, Stony Brook University, Stony Brook, NY 11794, USA

<sup>4</sup> Institute of Energy Technologies, Department of Chemical Engineering and Barcelona Research Center in Multiscale Science and Engineering, Universitat Politècnica de Catalunya, EEBE, Eduard Maristany 10-14, 08019 Barcelona, Spain

Corresponding Authors: Alessandro Trovarelli ([trovarelli@uniud.it](mailto:trovarelli@uniud.it)), Sara Colussi

([sara.colussi@uniud.it](mailto:sara.colussi@uniud.it)), Sanjaya Senanayake ([ssenanay@bnl.gov](mailto:ssenanay@bnl.gov))

## Abstract

The milling of Palladium acetate and CeO<sub>2</sub> under dry conditions results in robust, environmentally friendly catalysts with excellent methane oxidation activity. These catalysts show superior performance compared to those prepared by milling metallic Pd and outperform Pd/CeO<sub>2</sub> catalysts prepared by traditional incipient wetness technology. Morphological investigation by HRTEM, Raman and DRIFT spectroscopic analysis, *in-situ* synchrotron X-ray diffraction (XRD) and X-ray absorption fine structure (XAFS) characterization techniques, coupled with ambient pressure XPS analysis, have been used to deeply characterize the samples, and allowed to identify the presence of Pd<sup>0</sup>/Pd<sup>2+</sup> species with different degrees of interaction with ceria (Ce<sup>3+</sup>/Ce<sup>4+</sup>). These Pd species are likely generated by the mechanical and electronic interplay taking place over the ceria surface during milling and are indicated as responsible for the enhanced catalytic activity.

Keywords: mechanochemistry; methane; Palladium; ceria; oxidation.

## 1 Introduction

One of the main goals of the current research involving metal-oxide systems for catalytic applications is the optimization of the interaction between the metal and the support at the nanoscale level, due to its implications in the catalytic activity for different reactions [1–5]. In the case of metal-ceria formulations the strong interplay between the two components at the interface can lead to very interesting catalytic properties [6,7]. Recent studies have highlighted different aspects of metal-ceria interaction, with a significant amount of work dedicated to palladium-ceria systems for which a higher activity and/or stability is often observed when Pd is embedded or substituted into the ceria lattice. Pd/CeO<sub>2</sub> catalysts have been extensively investigated for the catalytic abatement of methane [8–17], and their peculiar characteristics have been also found promising for other reactions [18–23]. Theoretical investigations have given strong support to experimental results by demonstrating that various Pd-ceria embedded configurations are extremely stable and provide low energy barriers for CO and CH<sub>4</sub> molecular activation [24–28].

The synthesis of catalysts with strong metal-ceria interaction at nanoscale usually requires preparation methods in wet environment with subsequent thermal treatments, or methods which are not easily applicable at large scale [8,9,11,15]. We have recently reported a Pd/ceria catalyst prepared by simple dry milling of metallic Pd and CeO<sub>2</sub> powders, which showed increased catalytic

activity for methane oxidation with respect to an analogous sample prepared by traditional incipient wetness impregnation [14]. This improved activity was attributed to the formation of a mixed Pd-CeO<sub>2</sub> amorphous layer on the surface, closely resembling the structure predicted by DFT calculations in which the dissolution of palladium clusters into CeO<sub>2</sub> lattice yields a unique interface assembly with low methane activation barriers [27]. The enhancement of activity was found to be strongly dependent on the milling conditions showing that samples prepared under mild conditions were able to reach full conversion at low temperature compared to samples obtained by high energy milling [29]. The use of different metal precursors also affects the interaction between ceria and palladium and the preparation of Pd/CeO<sub>2</sub> using Pd acetate resulted in more robust and active catalysts [30]. Herein, a Pd/ceria formulation obtained by milling solid palladium acetate salt with ceria powder is investigated by varying Pd loadings and using CeO<sub>2</sub> support with a higher surface area and thermal stability [31–35]. The catalyst shows a morphology at nanoscale that resembles that observed on samples prepared using metal nanoparticles with an amorphous Pd-Ce-O shell surrounding ceria nanoparticles; however the distribution and characteristics of Pd/Pd<sup>n+</sup> species formed during reaction are unique leading to a highly active methane oxidation catalyst. Morphological investigation by HRTEM, Raman analysis, temperature programmed oxidation/reduction, *in-situ* synchrotron x-ray diffraction (XRD) and x-ray absorption fine structure (XAFS) characterization techniques, coupled with ambient pressure X-ray photoelectron spectroscopy and Fourier transform infrared spectroscopy, were used here to get deeper insights on the material and to identify the Pd active phase by closely following Pd-Ce interactions at a nanoscale level during reaction.

## 2 Experimental

**2.1 Synthesis of Pd-CeO<sub>2</sub> Catalysts.** Catalytic samples with a Pd loading of 1% and 4% by weight were prepared using Pd acetate salt (Pd(O<sub>2</sub>CCH<sub>3</sub>)<sub>2</sub>, Sigma Aldrich, 99.99%) and a commercial CeO<sub>2</sub> sample. Before Pd loading, CeO<sub>2</sub> was calcined at 1173 K (Ce1173) or at 1473 K (Ce1473) to obtain two supports with surface area/particle size of 23.4m<sup>2</sup>g<sup>-1</sup>/25nm and 3.8m<sup>2</sup>g<sup>-1</sup>/50nm respectively. 1 gram of powder with the appropriate amount of Pd acetate and CeO<sub>2</sub> was loaded in a 15 mL ZrO<sub>2</sub> grinding jar equipped with one ZrO<sub>2</sub> ball (ϕ15 mm), resulting in a ball-to-powder weight ratio (BPR) of 10. The two components were then milled in a Pulverisette 23 Minimill operating at 15 Hz in two subsequent 10-minute steps, separated by a manual mixing of the powder with a spatula inside the milling jar to avoid the formation of big agglomerates. The prepared samples were denoted as *x*PdAcCe(1173)M and *x*PdAcCe(1473)M, respectively, where *x* indicates

the nominal Pd loading. Reference samples were prepared by the previously reported mechano-chemical synthesis [14], using commercial Pd black and PdO nanopowders (Sigma Aldrich) as palladium precursors; these samples are denoted as  $x\text{PdCe}(1173)\text{M}$ ,  $x\text{PdCe}(1473)\text{M}$  and  $x\text{PdOCe}(1173)\text{M}$ . Another reference sample was prepared by conventional incipient wetness impregnation ( $x\text{PdCe}(1173)\text{IW}$ ,  $x\text{PdCe}(1473)\text{IW}$ ), following the state-of-the-art synthesis procedure. After wetting the ceria powders with the appropriate amount of an aqueous  $\text{Pd}(\text{NO}_3)_2$  solution (10 wt% in 10 wt% nitric acid, 99.999%, Sigma-Aldrich), the sample was dried at 373 K overnight and then calcined at 1173 K for 3 hours in static air. The choice of Pd precursor (nitrate vs acetate) for the mechano-chemical and IW syntheses was based on our previous work [30], where negligible improvement was observed by using  $\text{Pd}(\text{OAc})_2$  in IW preparation, in contrast with dry mechanical milling.

**2.2 Catalyst characterization.** All samples were characterized by means of BET surface area and pore size measurements, ICP-mass elemental analysis, High Resolution Transmission Electron Microscopy (HRTEM) and Temperature Programmed Oxidation (TPO) and Reduction (TPR) tests. The best performing samples with increased Pd loading were further characterized by means of Raman spectroscopy, synchrotron based *in-situ* XRD and XAFS measurements, ambient pressure X-ray photoelectron spectroscopy (AP-XPS) and diffuse reflectance infrared Fourier transform spectroscopy (DRIFTS). Surface area and pore size measurements were carried out in a Micrometrics Tristar Porosimeter by analyzing  $\text{N}_2$  adsorption isotherms at 77 K with the Brunauer-Emmett-Teller theory (BET) and Barrett-Joyner-Halenda method (BJH), respectively. ICP mass elemental analysis was performed to measure the actual metal loading on prepared samples. Microstructural characterization by high-resolution transmission electron microscopy (HRTEM) together with high angle annular dark-field (HAADF) scanning TEM (STEM) was performed on a field emission gun FEI Tecnai F20 microscope at 200 kV. TPO experiments were performed on 150 mg of catalyst placed in a quartz reactor and supported on a quartz wool bed. The sample was exposed to a flowing mixture (60 mL/min) containing 2 vol%  $\text{O}_2$  in  $\text{N}_2$ , and the oxygen release and consumption was monitored with an on-line ABB Magnos 106 paramagnetic analyzer during 3 heating/cooling cycles from RT up to 1273 K, at a heating/cooling ramp of 10 K/min. TPR experiments were carried out in a Micromeritics AutoChem II 2920 analyzer on 50 mg of catalyst loaded in a U-shaped quartz micro-reactor. The sample was cooled to 193 K in  $\text{N}_2$  by pumping liquid nitrogen on the outside wall of the reactor, then the temperature was ramped to 1233 K at a heating rate of 10 K/min under 35 mL/min of reducing mixture (4.5%  $\text{H}_2$  in  $\text{N}_2$ ). Before TPR samples were treated under air at 623 K for 1 hour.  $\text{H}_2$  consumption was monitored with a TCD detector. Quantification of hydrogen adsorbed was carried out by calibrating the apparatus with

reduction of known amount of CuO to metallic Cu. *Ex-situ* Raman spectra were collected with an Xplora Plus Micro-Raman system (Horiba, Kyoto, Japan) to evaluate the nature of PdO and CeO<sub>2</sub> structures on the catalysts after reaction. The samples were excited with the 532 nm radiation at room temperature and the spectra were acquired with a resolution of 1 cm<sup>-1</sup> and 5 accumulations of 60 s with a 50x LWD objective.

*In-situ* synchrotron x-ray diffraction was performed at Advanced Photon Source (APS), Argonne (IL), to follow the evolution of bulk Pd and PdO species during reaction. Time resolved XRD measurements were carried out at beamline 17BM with an energy of  $\lambda = 0.24169 \text{ \AA}$  using a Clausen cell flow reactor [36]. A 10 mL/min flow of gas mixture containing 0.5%CH<sub>4</sub>, 2%O<sub>2</sub> and 97.5% He for a 1:4 CH<sub>4</sub>:O<sub>2</sub> ratio was introduced and the temperature was then increased at 10 K/min to 773 K for two subsequent heating/cooling cycles; the first cycle was performed as a pretreatment. Two-dimensional images were collected continuously with a PerkinElmer Si flat panel detector through the reaction processes. The data were subsequently processed with the software GSAS-II [37].

*In-situ* XAFS measurements of Pd/CeO<sub>2</sub> catalysts were performed at 7-BM (QAS) beamline at National Synchrotron Light Source II (NSLS-II) of Brookhaven National Laboratory (BNL), Upton (NY). For methane oxidation experiments, the catalyst was stepwise heated from RT to 373 K, 473 K, 573 K and 673 K (20 min isothermal per step, 10 K/min heating ramp) under 10 mL/min flow of a 0.5%CH<sub>4</sub>, 2%O<sub>2</sub> in He gas mixture. A first heating/cooling cycle to 673 K was performed as pretreatment. The Pd K-edge data were collected in fluorescence yield mode using a passivated implanted planar silicon (PIPS) detector. Data processing was performed using the IFEFFIT package [38]. Pd foil was used as standard reference.

Ambient Pressure XPS analysis was performed with a commercial SPECS AP-XPS instrument equipped with a PHOIBOS 150 EPMCD-9 analyzer a Mg K $\alpha$  X-ray anode at the Chemistry Division of Brookhaven National Laboratory (BNL) to investigate the electronic states and evolution of the surface Pd and Ce species during reaction [39]. The powder catalysts were pressed on an aluminum plate, loaded into the AP-XPS chamber and pretreated at 673 K for 30 min under 20 mTorr O<sub>2</sub>. After cooling to room temperature, the chamber was evacuated and the reaction atmosphere was introduced through high-precision leak valves (10 mTorr CH<sub>4</sub>, 40 mTorr O<sub>2</sub>). O 1s, C 1s, Ce 3d and Pd 3d XPS regions were collected from RT to 673 K at a 100 K interval. The Ce 3d photoemission line with the strongest Ce<sup>4+</sup> feature (916.9 eV) was used for the energy calibration.

*In-situ* Diffuse Reflectance Infrared Fourier Transform Spectroscopy (DRIFTS) was carried out in a FTIR spectrometer (Bruker Vertex 70) equipped with a Harrick cell, MCT detector and mass

spectroscopy, to investigate the reaction intermediates during methane oxidation at low temperature and the palladium state under CH<sub>4</sub> or CO only. Before collection of the background, the catalyst was pretreated in 8%O<sub>2</sub>/He at 673 K for 1 hour. For methane oxidation tests, the background was collected at 573 K before the introduction of gas reactants (2% CH<sub>4</sub>/8% O<sub>2</sub>/He, 1:4 CH<sub>4</sub>:O<sub>2</sub> ratio). The gas flow was always balanced with helium to a total of 50 mL/min. For CO chemisorption tests, the background was collected in He at RT before the introduction of a 5%CO/He gas mixture for 10 min. The sample was subsequently purged in He for 30 min prior to spectra collection.

**2.3 Catalytic activity tests.** All samples were tested for complete methane oxidation in a lab-scale flow reactor setup. Temperature programmed combustion (TPC) tests were performed on 120 mg of sample loaded on a quartz wool bed inside a tubular quartz microreactor ( $\phi$ = mm). Brooks mass flow controllers were used to introduce 180 mL/min of a 0.5% CH<sub>4</sub>, 2%O<sub>2</sub> (balance He) gas mixture. The microreactor was inserted in a vertical tube furnace and heated from room temperature up to 1173 K at a linear rate of 10K/min and cooled to RT for two subsequent cycles. Cooling rate can be kept constant at 10K/min from 1173 to ca. 800K; at lower temperature slight deviation from this value can be observed. Reactants and products were continuously monitored with an on line ABB Uras 14 infrared gas analyzer coupled with an ABB Magnos 106 paramagnetic analyzer, and the temperature was measured with a K-type thermocouple placed at the top of the catalytic bed. The excess oxygen ensures full conversion of reagents into CO<sub>2</sub> and H<sub>2</sub>O, and methane conversion can be simply calculated as:

$$X_{CH_4}(\%) = \frac{CH_{4,t=0} - CH_{4,t}}{CH_{4,t=0}} \cdot 100$$

Stability tests, denoted as time-on-stream (TOS) tests, were performed by maintaining the sample at 723 K for 24 hours. TPC and TOS experiments were also carried out in “wet” conditions by adding 10 vol% of water vapor to the gas feed: 0.013 mL/min of liquid water were introduced with a Waters 515 HPLC pump and vaporized through heated lines. Reaction rates in dry atmosphere were calculated at methane conversion values  $\leq 5\%$  measured during the heating ramp of the 2<sup>nd</sup> light off cycle, in differential conditions [40–42].

### 3 Results

The surface area and Pd loading of the samples prepared on ceria support calcined at 1473 K and 1173 K are reported in Table 1. As expected, the surface area is low ( $\sim 4$  m<sup>2</sup>/g) for all samples prepared on Ce1473, with a slight increase for the milled samples containing 1 wt% of palladium,

likely due to the breakdown of bigger agglomerates into smaller particles during the milling process [43,44]. Ceria calcined at lower temperature (Ce1173) is characterized by higher surface area, ~25 m<sup>2</sup>/g, which is maintained on the milled samples while a significant loss is observed on 4PdCe(1173)IW. Indication of pore occlusion on this sample is observed by the analysis of pore size distribution, performed on desorption isotherms at 77 K using the BJH method (Figure S1). The measured Pd loading is close to the nominal one for all samples, except for the sample prepared using metallic Pd, where measured loading is lower than expected in agreement with our previous studies [14,29].

The result of the catalytic activity testing of sample 1PdAcCe(1473)M for lean methane oxidation is reported in Figure 1, in comparison with the light-off curves of the samples prepared by incipient wetness and by dry milling using Pd metal as precursor (1PdCe(1473)IW and 1PdCe(1473)M, respectively). The corresponding reaction rates calculated at 520 K are reported in Table 1.

**Table 1.** BET surface area, Pd loading and reaction rates of samples supported on ceria calcined at 1473 K and 1173 K.

<b>Sample</b>	<b>BET surface area (m<sup>2</sup>/g)</b>	<b>Pd loading (wt%)<sup>a</sup></b>	<b>Reaction rate (μmol/gPd·s)<sup>b</sup></b>
<b>CeO<sub>2</sub>(1473)</b>	3.8	-	-
1PdAcCe(1473)M	5.2	1.01	25.1
1PdCe(1473)M	4.8	0.81	14.1
1PdCe(1473)IW	3.7	0.97	6.4
4PdAc(Ce1473)M	3.1	4.03	8.5
4PdCe(1473)M	4.7	3.58	0.9
4PdCe(1473)IW	4.1	3.97	0.9
<b>CeO<sub>2</sub>(1173)</b>	23.4	-	-
4PdAcCe(1173)M	22.1	3.92	8.2 (31.3 <sup>c</sup> )
4PdCe(1173)M	25.1	3.69	0.7
4PdCe(1173)IW	14.6	3.94	3.3
4PdOCe(1173)M	26.7	3.83	n.d.

a: measured by ICP elemental analysis; b: measured at 520 K from the 2<sup>nd</sup> heating cycle of light-off curves; c: measured at 520 K from the 1<sup>st</sup> heating cycle of the light-off curve, following Pd(OAc)<sub>2</sub> decomposition.

The activity of the Pd metal-based and impregnated catalysts well compares with that of analogous samples, prepared on similar ceria support, already described in our previous papers [14,29]. As it can be observed, the use of palladium acetate as precursor significantly improves the overall catalytic activity, with a decrease of T<sub>10</sub> (temperature to achieve 10% methane conversion) of about 15 K, an almost double reaction rate at 520 K compared to 1PdCe(1473)M and a remarkable

improvement in conversion at high temperature in the cooling branch of the light-off curve. In particular, the typical loss in methane conversion usually present on Pd-based catalysts due to PdO-Pd transformation (and clearly visible for 1PdCe(1473)IW and 1PdCe(1473)M) is strongly reduced, the minimum being at a conversion of ca. 92% for 1PdAcCe(1473)M against 40-50% for the reference samples. The catalyst prepared from Pd acetate was tested also for stability over time-on-stream (Figure S2) and in presence of additional water in the feed (Figure S3a and S3b). In both cases the activity and stability of 1PdAcCe(1473)M are comparable, or even better than those of 1PdCe(1473)M which, in turn, was found to be superior to the conventional impregnated sample.

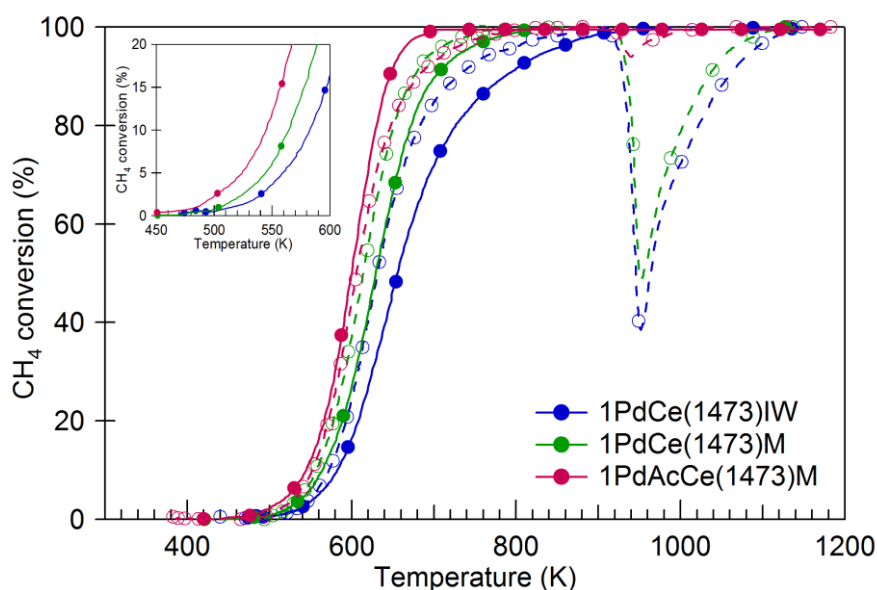


**Figure 1.** Methane oxidation activity of samples 1PdAcCe(1473)M, 1PdCe(1473)M and 1PdCe(1473)IW. Inset: focus on the 450-600 K light-off activity. Solid line, closed symbols: heating; dashed line, open symbols: cooling.

Increasing Pd loading up to 4 wt% significantly enhances the overall conversion of methane on PdAcCe(1473)M, and it is worth noting that in this case, there is no loss in methane conversion during cooling (Figure 2). On the other side, the higher Pd loading is detrimental for samples prepared by wet deposition and by milling Pd metal and ceria: light-off and conversion behavior of 4PdCe(1473)M and 4PdCe(1473)IW are negatively affected compared to samples at lower loadings (Figure S4a and b, respectively). This is also clearly observed by reaction rates that drop by one order of magnitude. The preparation of 4 wt% Pd catalysts on ceria calcined at 1173 K (S.A. ca. 25 m<sup>2</sup>/g) slightly improves the activity of the impregnated sample and of the one obtained by milling with metallic Pd, both remaining well below the activity of 4PdAcCe(1173)M (Figure 3), which does not seem to be affected by the surface area of the support. The use of Pd acetate as Pd

precursor allows to introduce up to 10 wt% of palladium on ceria calcined at 1173 K without any loss of conversion in light off curves (Figure S5).

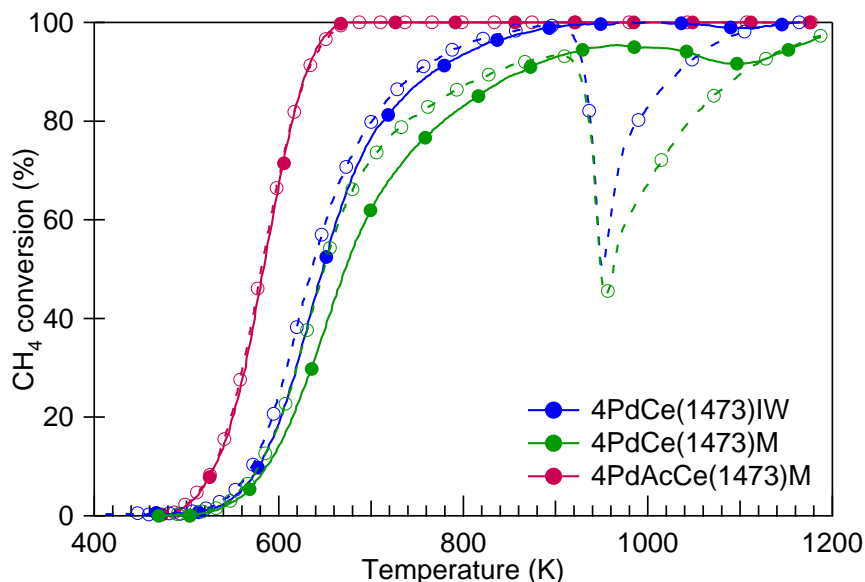


**Figure 2.** Methane oxidation activity for 4wt%Pd/CeO<sub>2</sub> samples on CeO<sub>2</sub> calcined at 1473 K. Solid line, closed symbols: heating; dashed line, open symbols: cooling.

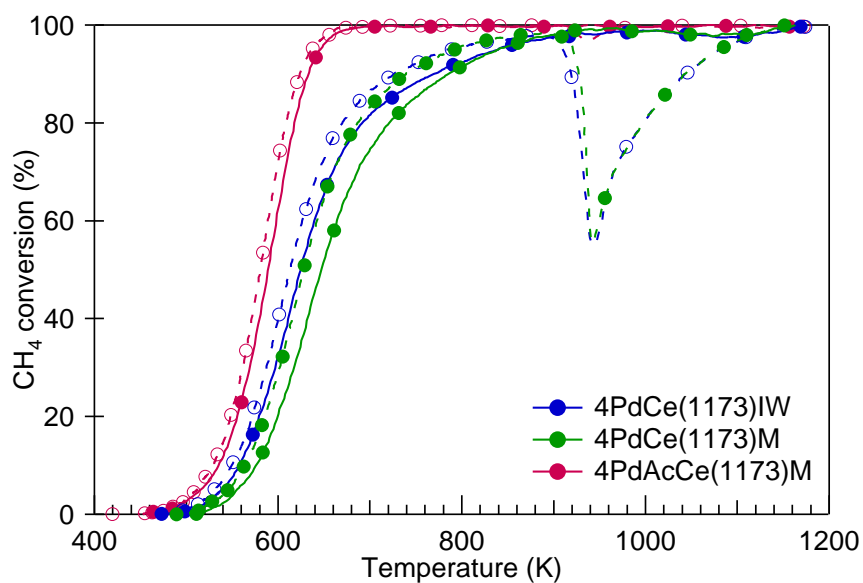


**Figure 3.** Methane oxidation activity of 4wt%Pd/CeO<sub>2</sub> samples on CeO<sub>2</sub> calcined at 1173 K. Solid line, closed symbols: heating; dashed line, open symbols: cooling.

A general view in STEM mode of 4PdAcCe(1173)M (Figure S6) shows a homogeneous distribution of ceria crystallites with rounded edges with no segregated palladium entities, indicating that the noble metal is well-dispersed over the ceria support. In HRTEM images, presented in Figure 4, CeO<sub>2</sub> particles with rounded edges can be clearly distinguished. The

amorphous nature of the shell (marked by arrows) over the ceria crystallites is clearly seen, measuring about 1-2 nm in thickness.

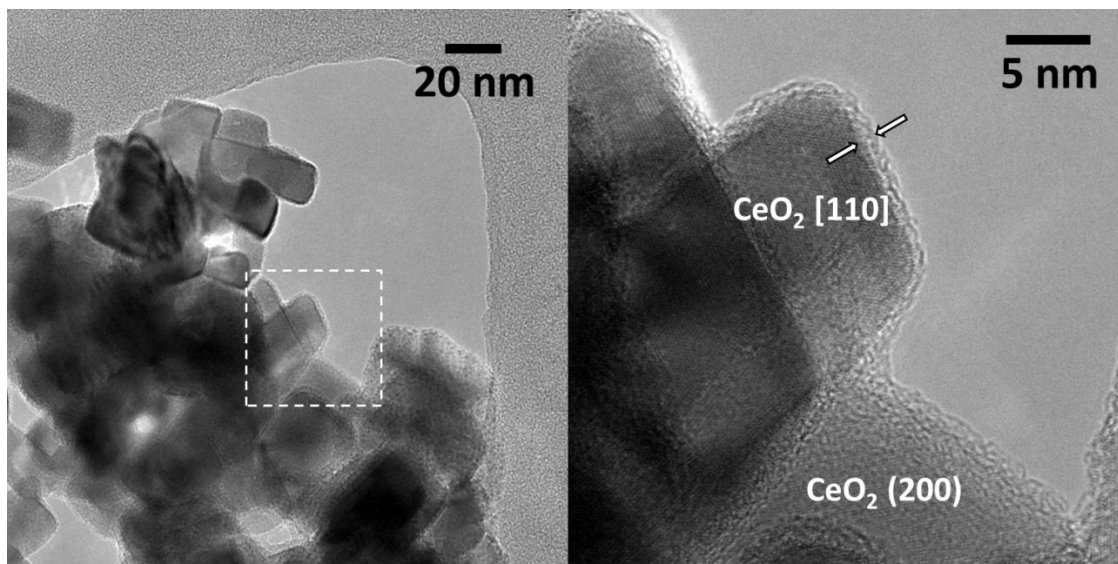


**Figure 4.** HRTEM images of 4PdAcCe(1173)M exhibiting an amorphous layer uniformly covering the ceria crystallites.

The arrangement of Pd on the surface is highlighted in Figure 5. In Figure 5A darker subnanometric entities on the ceria surface can be identified, indicated by arrows. By careful analysis of the HRTEM images and through intentional defocus, the entities can be recognized to occur at the surface of the ceria crystallite and are not to be confused with artifacts originating from the thickness of the particle and/or the carbon film of the TEM grid. It can be estimated that the size of the entities is below 0.5 nm and their higher electron contrast indicates they probably contain Pd. Figure 5B corresponds to a higher magnification image of the same particle, showing (200) planes of ceria along with defocused entities on the surface that can be estimated below 0.5 nm in size. Figure 5C shows an HRTEM image resolved at an atomic scale. The ceria crystallite is oriented along the [112] crystallographic direction. In addition to the lack of well-defined edges of the ceria crystallite, the atomic rows located at the outermost surface look striking. Despite the impossibility to extract any definitive conclusion, the dark rows located just at the surface and parallel to the {111} steps of the crystallite (marked by black arrows) might indicate the presence of a monolayer of Pd atoms or Pd islands. These rows are slightly bended outwards the surface, suggesting that they are not due to the ceria lattice. At the surface of the {220} face other dark rows are recognized (marked by white arrows). In Figure 5D, the darker nanostructures over the ceria crystallites are identified as PdO as deduced from the lattice fringes at 2.6 and 1.7 Å, corresponding to the

characteristic (101) and (112) planes of tetragonal PdO. These PdO nanostructures are crystalline and measure about 1-1.5 nm in diameter and are very well dispersed over CeO<sub>2</sub>. This architecture is found over the entire sample, with no Pd agglomeration in any case.

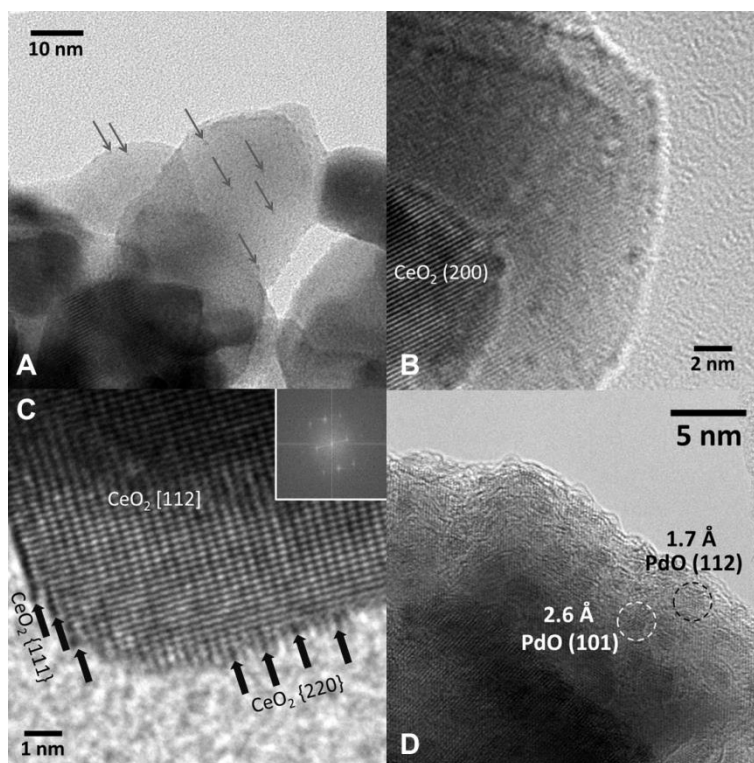


**Figure 5.** HRTEM images of the different Pd species observed on 4PdAcCe(1173)M after one reaction cycle up to 1173 K: sub-nanometric Pd entities well dispersed on the ceria surface (A,B), palladium ions inserted in the outermost ceria lattice (C), round PdO entities measuring ca. 2 nm and exhibiting (101) and (112) planes, in addition to a thin amorphous layer (D).

Samples 4PdCe(1173)IW and 4PdCe(1173)M exhibit a rather different morphology. A general view of the samples in STEM mode is presented in Figure S7, where the presence of Pd agglomerates and Pd nanoparticles in addition to ceria crystallites can be clearly observed. 4PdCe(1173)M shows abundant starting Pd metal nanoparticles segregated from ceria. In addition, an amorphous shell around ceria crystallites and PdO nanostructures measuring 0.5 nm in size are also present, but most of the Pd nanostructures occur as PdO flake-like monolayer nanostructures of about 1-3 nm in length. The sample prepared by impregnation contain well-dispersed Pd nanoparticles of about 1.5-2 nm in size anchored over well-faceted ceria crystallites (Figures S8 and S9).

The presence of different Pd species on 4PdAcCe(1173)M can also be inferred from TPO experiments, and particularly from the oxygen release portion of the profile (Figure 6). Oxygen evolution in 4PdAcCe(1173)M sample is very broad and less defined if compared to 4PdCe(1173)IW and 4PdCe(1173)M, indicating the existence of more Pd and/or oxygen species

linked to Pd with different degree of stability. In addition, on 4PdAcCe(1173)M there is a higher fraction of PdO decomposing at higher temperature, while the IW sample displays a single broad peak centered at around 1060 K. On 4PdCe(1173)M, a well-defined O<sub>2</sub> release peak is observed at low temperature and a lower amount of cycling palladium is highlighted by the quantitative analysis of oxygen consumed and released, reported in Table 2.

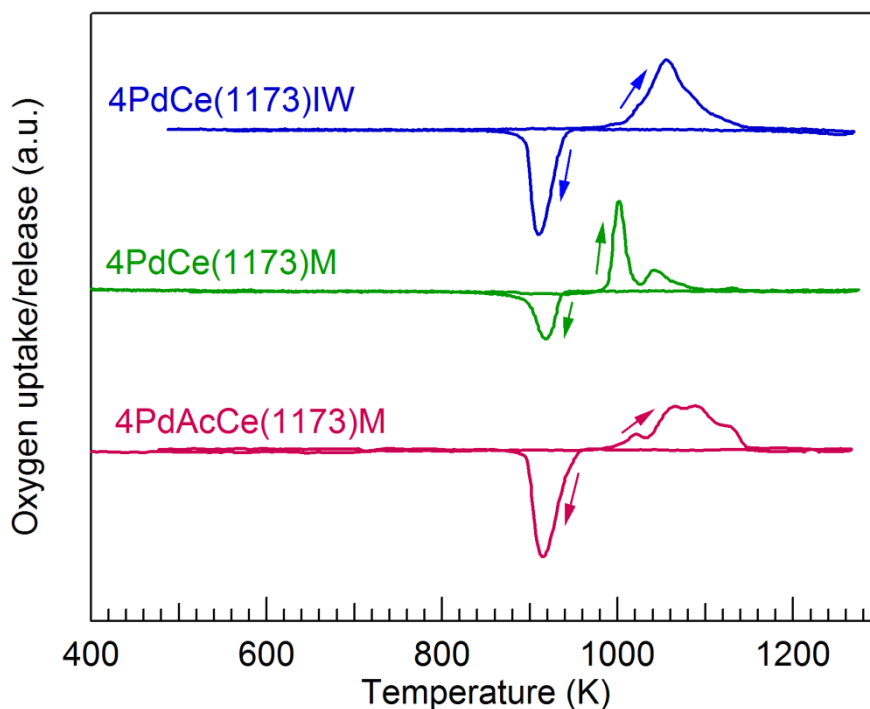


**Figure 6.** Oxygen uptake/release profiles in TPO for 4wt%Pd/CeO<sub>2</sub>(1173) samples, 3<sup>rd</sup> heating/cooling cycle.

**Table 2.** Quantitative analysis of TPO profiles, 3<sup>rd</sup> heating/cooling cycle.

Sample	Measured Pd loading (wt%)	O <sub>2</sub> release (μmoles O <sub>2</sub> /g) <sup>a</sup>	O <sub>2</sub> uptake (μmoles O <sub>2</sub> /g)
4PdCe(1173)IW	3.94	147.6 (80)	123.2 (67)
4PdAcCe(1173)M	3.92	140.3 (76)	133.9 (73)
4PdCe(1173)M	3.69	95.5 (55)	75.1 (43)

a: the amount of Pd (% of total Pd) that is involved in oxidation/decomposition is reported in parentheses.

The nature of palladium particles formed on 4%Pd/CeO<sub>2</sub>(1173) samples can also be inferred from H<sub>2</sub>-TPR profiles. The evolution of hydrogen consumption at low temperature is related to the reduction of PdO particles to Pd and PdH<sub>y</sub> [45,46], which occurs at around 260-270 K on the milled samples and at 290 K on 4PdCe(1173)IW (peak α in Figure 7). Due to the complex redox behavior of supported palladium catalysts, in the literature there is no general agreement on the specific

attribution of reduction peaks in such a narrow temperature range (260-320 K). As a general rule, most studies attribute reduction peaks at low temperature to small PdO particles and/or PdO<sub>x</sub> species well dispersed on the support [47,48], while the H<sub>2</sub> uptake at higher temperature is linked to larger particles and palladium species with stronger interaction with the support [45]. At the same time, low temperature reduction peaks with H<sub>2</sub> consumption above the stoichiometric amount, such as the ones observed on the milled samples, are generally attributed to a stronger H<sub>2</sub> spillover effect of noble metals on ceria or on ceria-based support [49]. The subsequent H<sub>2</sub> release at 333 K (peak β) is generally attributed to the decomposition of palladium hydride species, whose formation is promoted on large PdO particles [48,50]. The semi-quantitative analysis of the TPR profiles, reported in Table 3, shows that both 4PdCe(1173)M and IW samples display a more significant H<sub>2</sub> release feature compared to 4PdAcCe(1173)M, suggesting that larger PdO particles are present on their surface. The reduction of bulk ceria (peak γ) does not appear to be affected by the preparation route.

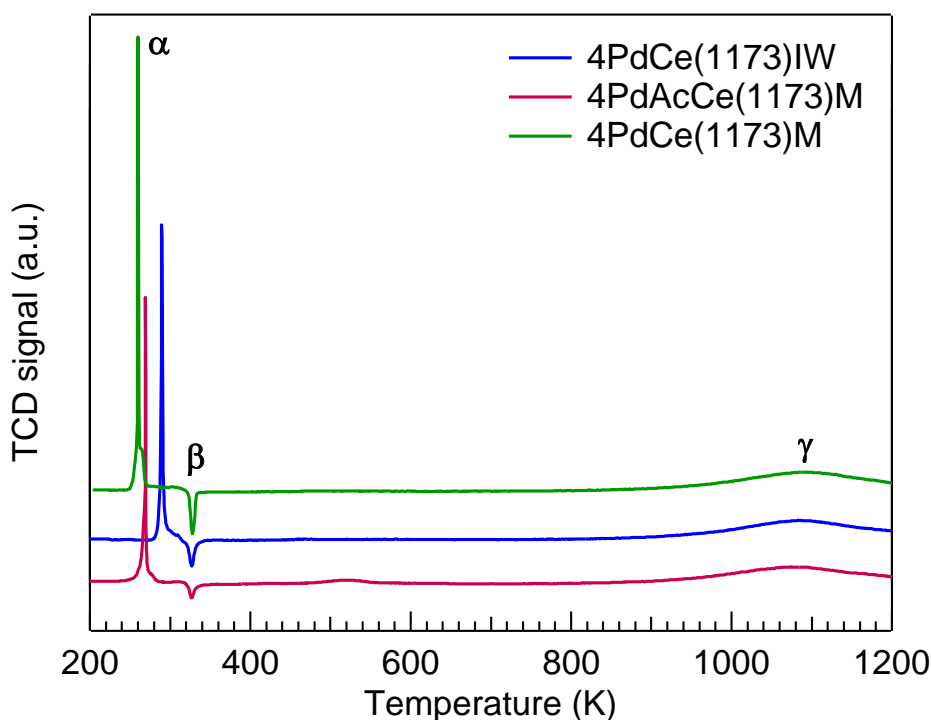


**Figure 7.** H<sub>2</sub>-TPR profiles of 4wt%Pd/CeO<sub>2</sub>(1173) samples.

**Table 3.** Theoretical and calculated hydrogen consumption during H<sub>2</sub>-TPR tests on 4wt%Pd/CeO<sub>2</sub>(1173) samples (μmol H<sub>2</sub>/g).

Sample	H <sub>2</sub> uptake for stoichiometric PdO reduction	Peak α	Peak β	Peak γ
4PdCe(1173)IW	370	448	66	568
4PdAcCe(1173)M	368	419	44	573

<b>4PdCe(1173)M</b>	347	460	75	667
---------------------	-----	-----	----	-----

A more detailed analysis of the nature of Pd in 4PdAcCe(1173)M has been undertaken through *in-situ* and other spectroscopic techniques. The surface palladium species and electronic states were evaluated and compared to the reference 4PdCe(1173)IW. It should be highlighted that in this study the advanced characterization carried out with the help of synchrotron light techniques has involved typically the temperature range in which methane activation takes place (423-773 K), with the aim of understanding the role of different Pd-ceria arrangements, whereas the investigation of the high temperature behavior and stability of the samples is beyond the scope of the present work.

*In-situ* synchrotron X-ray diffraction analysis was carried out on the milled and the impregnated samples, performing two subsequent heating/cooling cycles up to 773 K under lean reaction mixture (see Scheme S1). Comparative methane oxidation tests were performed in a lab-scale reactor setup to evaluate the catalytic activity of samples in a Clausen Cell under reaction conditions (heating ramp up to 773 K, GHSV  $\approx$  400'000 h<sup>-1</sup>) (Figure S10). At higher space velocity, on 4PdAcCe(1173)M methane conversion starts slightly before 500 K and full conversion is reached at 673 K, outperforming the reference 4PdCe(1173)IW sample that lights off at ca. 570 K.

In Figure 8 the *in-situ* XRD profiles of 4PdCe(1173)IW (a,c) and 4PdAcCe(1173)M (b,d) are reported, showing the time-resolved evolution of ceria (Figure 8a,b) and of the palladium species (Figure 8c,d) under reaction conditions. The presence of mostly crystalline PdO together with a small metallic Pd feature can be inferred for the impregnated catalyst (Figure 8c). Conversely, on the milled sample broader and less intense Pd and PdO peaks are detected in the whole temperature range after the decomposition of palladium acetate, indicating a smaller palladium particle size and a higher degree of metallic Pd in coexistence with PdO (Figure 8d). Representative diffractograms and reference diffraction patterns for Pd and PdO phases are reported in Figure S11. On both samples, the size of the ceria crystallites remains constant throughout reaction (Figure 8a,b). The same is observed for methane oxidation on pure ceria and on 4PdOCe(1173)M (Figure S12). On the latter, PdO nanoparticles are extremely small, initially escaping detection and then gradually undergoing sintering during methane oxidation pretreatment at around 673 K. Rietveld refinement of the XRD diffractograms does not reveal any substitution of Pd into CeO<sub>2</sub> lattice for any of the samples, the variation in the lattice parameter being due only to thermal expansion. This can be inferred from the comparison of the variation in the lattice parameter of Pd-containing samples with that of pure CeO<sub>2</sub> subjected to the same *in-situ* characterization (Figure S13). Rietveld refinement

of the supported metal species on 4PdAcCe(1173)M is challenging due to the small peak size of Pd and PdO, while on 4PdCe(1173)IW an average PdO particle size of 5 nm can be calculated.

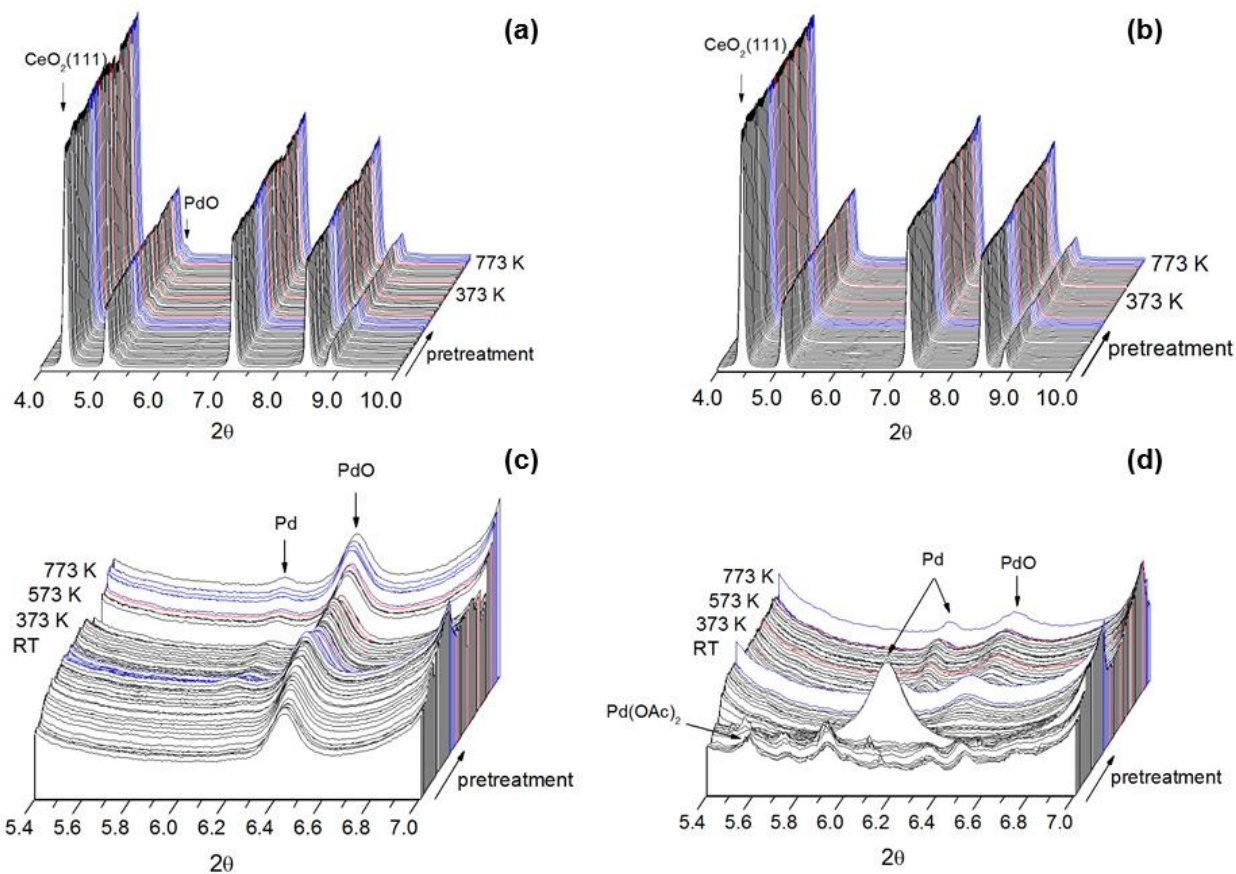


**Figure 8.** *In-situ* synchrotron XRD diffractograms of 4PdCe(1173)IW (a,b) and 4PdAcCe(1173)M (b,d). Full time-resolved patterns show the evolution of CeO<sub>2</sub> (a,b) and of palladium species (c,d). Red lines indicate significant reaction temperatures, blue lines represent cooling, first heating ramp to 773 K is the pretreatment.

The presence of a higher amount of crystalline PdO on 4PdCe(1173)IW was confirmed by Raman spectroscopy. Prior to Raman characterization, the samples were exposed to the reaction mixture up to 773 K, to mimic the experimental conditions of *in-situ* XRD; representative spectra of the milled and impregnated catalysts are reported in Figure 9. In addition to the characteristic peaks at 461 cm<sup>-1</sup> and at 646 cm<sup>-1</sup>, corresponding to the F<sub>2g</sub> mode of CeO<sub>2</sub> and the B<sub>1g</sub> vibrational mode of PdO, respectively, the spectra in Figure 9 highlight a broad band between 550 and 600 cm<sup>-1</sup> on 4PdAcCe(1173)M, suggesting that a higher degree of ceria lattice defects are present on its surface [51]. Mapping of the catalysts further shows that the IW sample presents a higher amount of crystalline PdO structure on the surface with respect to 4PdAcCe(1173)M, coherently with XRD

results (Figure S14). In fact, the Raman signal originates from the symmetric stretching of the O-Pd-O bond in a PdO<sub>4</sub> configuration [25,52], which is mostly found in the core of crystalline particles. The lower intensity of the PdO B<sub>1g</sub> signal on the milled sample might be ascribed to smaller domains of palladium oxide as well as to the amorphous shell structure.

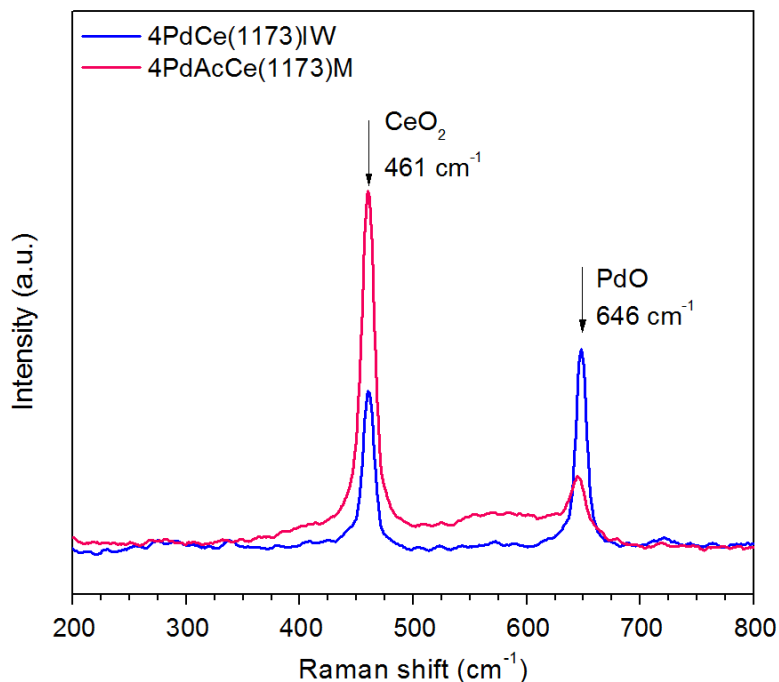


**Figure 9.** Raman spectra collected on 4PdCe(1173)IW and 4PdAcCe(1173)M after methane oxidation test up to 773 K.

The arrangement of Pd species on 4PdCe(1173)IW and 4PdAcCe(1173)M was followed by *in-situ* XAFS measurements. Figure 10 shows XANES (Figure 10a) and EXAFS (Figure 10b) profiles for the samples after pretreatment and at 673 K during reaction. EXAFS analysis of the spectra collected before reaction are shown in Figure S15, while the full time-resolved XANES spectra, showing minimal changes throughout reaction in the evaluated temperature range (300-673 K), are reported in Figure S16. A more careful analysis of the XANES profiles recorded at RT and at 673 K, reported in Figure 10a, highlights a more reduced state on the milled sample compared to the IW catalyst, maintained during reaction. This is also reflected in the R space (Figure 10b), where on 4PdAcCe(1173)M a first peak at the Pd-O shell (at  $\sim 1.6\text{\AA}$ ) is detected along with a contribution at  $2.5\text{\AA}$ , corresponding to the metallic Pd-Pd shell. On 4PdCe(1173)IW, more pronounced peaks at the Pd-O ( $\sim 1.6\text{\AA}$ ) and Pd-Pd<sub>2</sub> ( $\sim 3\text{\AA}$ ) shells are measured, corroborating the existence of larger Pd-O contribution and, consequently, a more oxidized Pd environment on the sample prepared by incipient wetness impregnation. The absence of the Pd-Pd<sub>2</sub> shell on the reference PdO is due to the small particle size of the PdO nanoparticles used as standard.

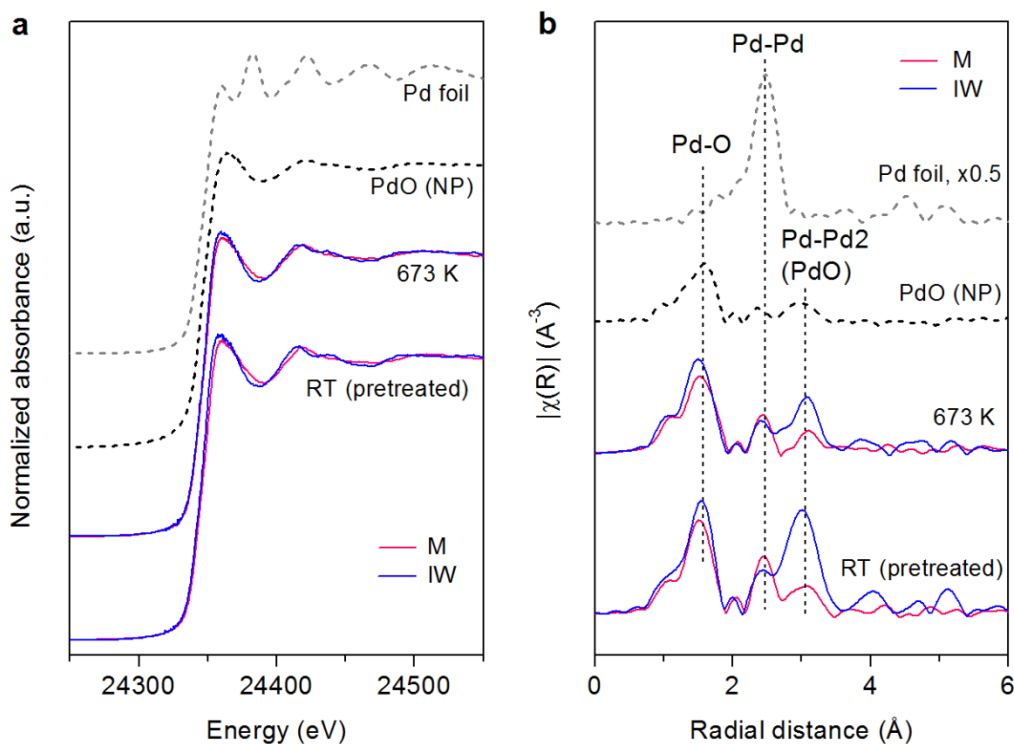


**Figure 10.** *In-situ* Pd K-edge XANES (a) and EXAFS (b) data of 4PdCe(1173)IW and 4PdAcCe(1173)M catalysts recorded at room temperature after one methane oxidation cycle (pretreated) and under reaction conditions at 673 K. Spectra of Pd foil and PdO nanoparticles (NP) are reported as reference.

The oxidation state of palladium and ceria during low temperature methane oxidation was followed by *in-situ* Ambient-Pressure X-ray Photoelectron Spectroscopy (AP-XPS) experiments. While both samples display a relatively stable state throughout the whole temperature range (RT to 673 K), as shown in Figure 11, a remarkable difference in palladium oxidation states can be observed. On the IW catalyst the spectra collected in the Pd 3d region demonstrate that palladium is present mostly in an oxidized and super-oxidized state ( $\sim 25\%$  Pd<sup>2+</sup> and 70% Pd<sup>4+</sup>) with traces of Pd<sup>0</sup> (<5%). Conversely, on the dry milled sample (Figure 11b) surface Pd<sup>2+</sup> species are predominant, accompanied by metallic Pd<sup>0</sup> species (between 5-20%) with a maximum amount recorded at the lowest temperatures (373 K). The transformations of palladium species are accompanied by minor changes of surface ceria, exhibiting a slightly more reduced state on 4PdCe(1173)IW than on the milled sample, as shown by the calculated  $x$  in CeO <sub>$x$</sub>  in Figures 11a and b, respectively. Representative Pd 3d and Ce 3d spectra are reported in Figure 12, highlighting a strong Signal-to-Noise Ratio (SNR) for Pd 3d on 4PdAcCe(1173)M and for Ce 3d on 4PdCe(1173)IW. On the milled sample the strong Pd signal indicates an improved dispersion of palladium on the ceria surface with a Pd/Ce atomic ratio of 2.45, while on the IW catalyst the surface Pd/Ce ratio is only

equal to 0.34, hence suggesting a large amount of bare ceria surface. The full evolution of collected spectra as a function of temperature and the calculated atomic fractions are reported in Figure S17 and Table S1, respectively.

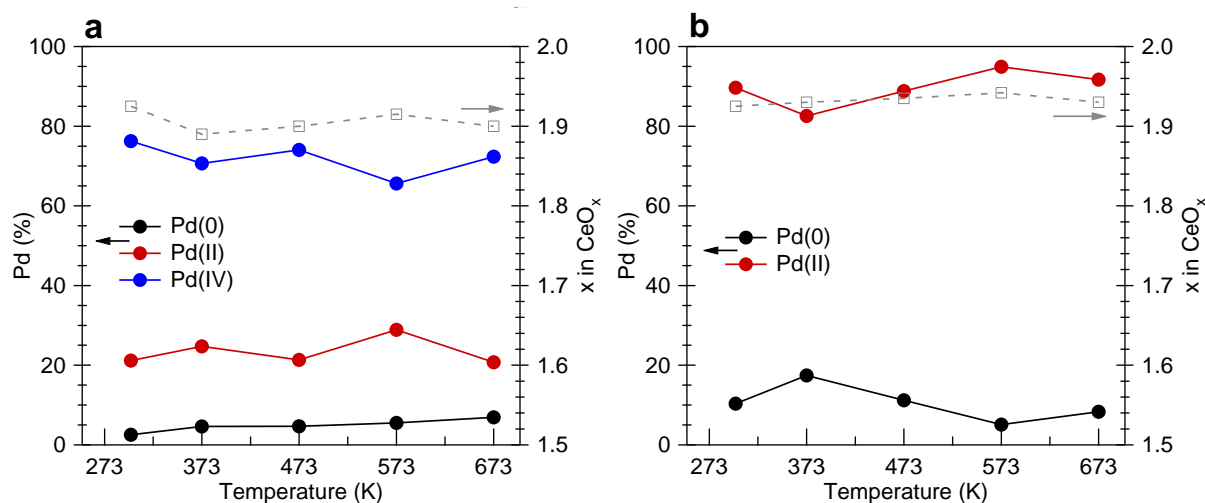


**Figure 11.** Evolution of the Pd and Ce oxidation states as measured by AP-XPS analysis of Pd 3d and Ce 3d regions on 4PdCe(1173)IW (a) and 4PdAcCe(1173)M (b) during methane oxidation tests. Solid line, full circles: Pd (left axis); dashed line, open squares: calculated  $x$  in  $\text{CeO}_x$  (right axis).

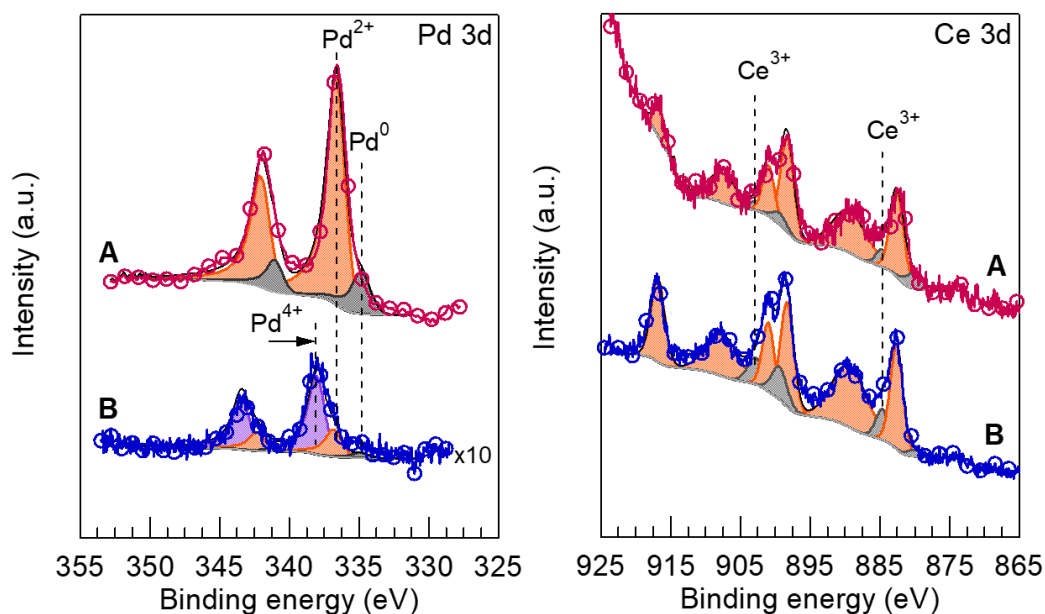


**Figure 12.** AP-XPS spectra collected in the Pd 3d and Ce 3d regions on 4PdAcCe(1173)M (A) and 4PdCe(1173)IW (B) at 373 K under 10 mTorr  $\text{CH}_4$ , 40 mTorr  $\text{O}_2$ .

The transformations occurring on the surface and the nature of Pd species have been followed also by *in-situ* DRIFTS analysis. Methane oxidation tests were carried out in isothermal conditions at 573 K; an intermediate  $\text{O}_2$ -removal step was performed to investigate the methane activation

reactivity and the activity recovery following O<sub>2</sub> re-introduction. Experimental conditions have been chosen to optimize the *in-situ* measurements in the apparatus (reported in detail in Scheme S2).

The most significant spectra collected on 4PdAcCe(1173)M and 4PdCe(1173)IW after 30 minutes of each reaction step (first methane oxidation step, methane-only after O<sub>2</sub> removal, second oxidation step) are compared in Figure 13a. The reaction evolution can be followed by formation of gaseous CO<sub>2</sub> (band at 2350 cm<sup>-1</sup>), which disappears under CH<sub>4</sub>-only conditions and is more intense on 4PdAcCe(1173)M. After oxygen is removed, the formation of carbonate species on ceria occurs and it is strongly promoted on the sample prepared by incipient wetness, as inferred by the broad peaks around 1600-1500 cm<sup>-1</sup> and 1350 cm<sup>-1</sup> [53–55]. These species quickly disappear on the milled sample when oxygen is re-added to the gas feed, while on 4PdCe(1173)IW they are removed slowly and some can still be observed after 30 minutes under oxidizing condition.

A closer look at the region of CO-bonds on palladium (2100-1800 cm<sup>-1</sup>, Figure 13a) reveals that, during the reduction in methane, PdO is reduced to large metallic Pd particles on both samples, resulting in intense bands at 1900 and 1800 cm<sup>-1</sup> due to bridge and hollow CO on Pd(111) [54,56–58], with more Pd available on the surface of the milled catalyst. In addition, a band at about 2050 cm<sup>-1</sup> is also observed on 4PdAcCe(1173)M, which might be attributed to CO linearly bonded to metallic Pd or to oxygen vacancies (O<sub>v</sub>) near undercoordinated PdO (101) planes [58,59]. This is further confirmed by CO chemisorption tests (Figure 13b), where the band at 2090 cm<sup>-1</sup> is especially evident on the milled sample.

The full evolution of adsorbed species is reported in Figure S18(a,b), together with the spectra collected on pure ceria (Figure S18c). On the Pd/CeO<sub>2</sub> catalysts, the reduction of PdO during the treatment under CH<sub>4</sub> can be observed by the shift in the background due to the formation of darker metallic Pd. This transition is much faster for the milled sample compared to the reference IW catalyst. On pure CeO<sub>2</sub> no reaction occurs, as expected, and carbonate species are formed on the ceria surface during the first methane oxidation step (bands at 1545 and 1355 cm<sup>-1</sup> [53,54], Figure S18c). A summary of the main frequencies of interest and their assigned species from the literature is reported in Table 4.

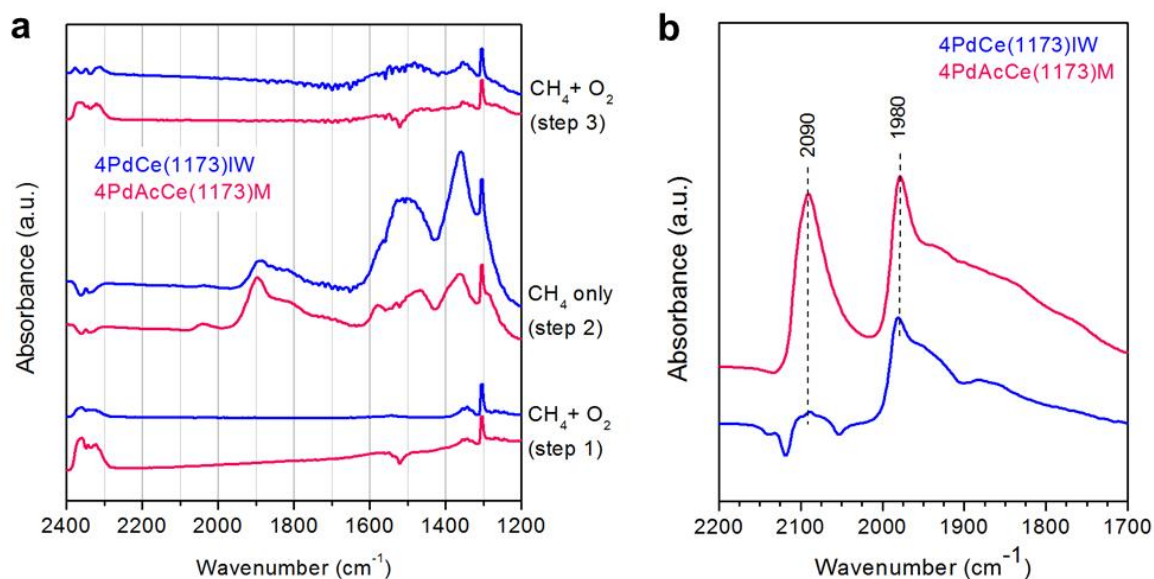


**Figure 13.** (a) Comparison of DRIFTS spectra recorded on 4PdAcCe(1173)M and 4PdCe(1173)IW during isothermal methane oxidation test at 573 K after 30 min exposure in reaction conditions (step 1), methane only (step 2), and second reaction step (step 3) (see Scheme S2). (b) DRIFTS spectra recorded after CO chemisorption; spectra were collected at RT after introduction of a 5%CO/He gas mixture for 10 min and a subsequent purge in He for 30 min.

**Table 4.** Assignments of the main IR bands observed during methane oxidation and CO-chemisorption tests.

Frequency (cm <sup>-1</sup> )	Assignment	Reference
2350	CO <sub>2,gas</sub>	[54]
1305	CH <sub>4,gas</sub>	[60,61]
2085	CO-O <sub>v</sub> -PdO(101)	[59,62]
2090-2034	CO-Pd <sup>0</sup> linear	[54,56,59]
1980-1890	CO-Pd <sup>0</sup> bridged	[54,56,57,63]
1577-1519,1353	carbonates	[53,54]

## 4 Discussion

The milling of palladium acetate with low surface area cerium oxide powders results in highly active methane oxidation catalysts, displaying a remarkable low temperature activity. These catalysts also show a significant reduction in the activity loss at high temperature during the heating and cooling branches of the light-off curve (Figure 1). The loss of activity at high temperature is linked to the dynamics of PdO-Pd decomposition [64]. To our best knowledge, a decrease in the activity loss during the cooling branch of the light-off cycle on Pd-based catalysts was reported only in a few recent works [9,65,66], in which stability of palladium species was achieved by means of

Pd@CeO<sub>2</sub> units supported on alumina or atomic layer deposited Al<sub>2</sub>O<sub>3</sub> overlayers on Pd particles supported on SiO<sub>2</sub>. In both cases, the authors attributed the improved performance to the Pd core-support oxide shell configuration able to maximize the metal-support interface and stabilize the PdO/PdO<sub>x</sub> active phase at high temperature. Here the optimization of metal-support interface occurs through an opposite physical arrangement, where an inner CeO<sub>2</sub> core is surrounded by an outer Pd-CeO<sub>2</sub> shell. From TPO experiments (Figure 6 and Figure S19a) it appears that the PdO-Pd transformation still occurs on these samples, indicating that the reduction in activity in the high temperature cooling branch is likely due to their overall superior performance with respect to conventional catalysts. As a matter of fact, comparing methane oxidation tests carried out at higher space velocity (GHSV  $\approx 2 \cdot 10^6$  h<sup>-1</sup>) the characteristic activity drop at high temperature can be clearly observed during cooling (Figure S20).

Experiments carried out at increasing Pd loading show that samples prepared by milling Pd acetate are able to successfully accommodate higher metal loading. Figures 1-3 and Figure S4 and S5 show catalytic activity on 1-10 wt% Pd deposited on supports with different degree of thermal sintering. Results indicate that PdAc/CeO<sub>2</sub> milled samples are able to accommodate up to 10% wt. of Pd in very active configurations. On the other hand, increasing the loading of Pd from 1 to 4 wt.% in samples prepared by incipient wetness and in samples milled with Pd metal results in less performant samples (Figure 2), showing that ceria cannot efficiently accommodate higher metallic Pd loadings, as inferred also by comparing the light-off curves of 1 wt% and 4 wt% PdCe(1473)M (Figure S4). The use of a ceria support with higher thermal stability and, consequently, a higher surface area at high temperature improves only partially the overall catalytic activity for the samples prepared by impregnation or by milling with metallic Pd (Figure 3).

The reason for the different behavior of milled *vs* IW samples and of samples milled with acetate and with Pd metal powder must be correlated to the different arrangement of the active metal phase at nanoscale. The most recent experimental and theoretical works investigating the catalytic activity for methane oxidation of Pd-based catalysts clearly indicate that there are specific Pd-O configurations, such as ionic Pd species and/or particular Pd-PdO exposed facets, that are more effective in methane activation [16,60,67,68], and this is true also when considering ceria-supported Pd catalysts [27,69]. The characterization carried out in this work allowed to understand that the catalysts obtained from Pd acetate present a larger variety of Pd species, which appear to be responsible for its enhanced methane oxidation activity.

Morphological characterization of these samples by HRTEM shows a uniform distribution of palladium clusters on 4PdCe(1173)IW, highly crystalline and with an average size of ca. 2 nm

(Figure S8), while 4PdCe(1173)M presents a non-homogeneous Pd distribution with the presence of isolated particles, flake-like features and limited regions of amorphous shell structure (see Supplementary, Figure S9). It is evident that the dry milling synthesis using metallic Pd as precursor, which was very effective at 1wt% loading, is not able to successfully distribute higher (4 wt%) Pd content on the ceria surface (Figure S4). Conversely, the use of palladium acetate enables the successful deposition of higher loadings of Pd on CeO<sub>2</sub> (Figure S5) through the formation of a variety of Pd species on the ceria surfaces, as observed by HRTEM images in Figure 5. In addition to a thin amorphous layer, additional smaller palladium entities can be identified on ceria: some are below 0.5 nm and appear as sparse darker spots, some are larger (1-2 nm) and exhibit planes of tetragonal PdO. The insertion of Pd atoms in the outermost ceria lattice is also suggested. TPO profiles (Figure 6) confirm the existence of multiple Pd species on 4PdAcCe(1173)M with several degrees of interaction with ceria support, compared to predominant bulk PdO species on 4PdCe(1173)IW [70]. The higher degree of Pd oxidation on the impregnated sample is confirmed also by XPS, XANES and EXAFS results (see below). On 4PdAcCe(1173)M there is a higher fraction of PdO decomposing at higher temperature, usually indicating the presence of PdO<sub>x</sub> species in stronger interaction with the support [70], but the presence of other PdO species in weaker interaction with ceria is also inferred from the analysis of TPO profiles. This might explain the formation of relatively large Pd(111) domains observed by DRIFTS during CO and CH<sub>4</sub> reduction.

The heterogeneous mixture of Pd species likely stems from the Pd<sup>0</sup>/Pd<sup>2+</sup> mixture created after decomposition of palladium acetate during pretreatment, as recently reported [30] and further observed by *in-situ* XRD (Figure 8d). Such sub-stoichiometric Pd<sup>0</sup>/Pd<sup>2+</sup> mixture is stabilized by the amorphous ceria surface structure, induced during mechanical milling by the creation and accumulation of defects [71]. The substitution of Pd into the ceria lattice is not detected by Rietveld refinement of the *in-situ* XRD spectra, but its local occurrence inside the amorphous shell cannot be excluded [25], as the shell/bulk volume ratio identified by HRTEM is very small and the bulk CeO<sub>2</sub> signal could prevent its detection. Such a disordered nanoscale environment might promote oxygen transfer, thus enabling faster methane oxidation turnover, reducing the inhibition effect of steam, concurring to the faster removal of carbonates observed during DRIFTS “on-off” oxidation tests and improving reducibility of Pd species, as observed both during H<sub>2</sub>-TPR tests (Figure 7) and under CH<sub>4</sub> only DRIFTS experiments (Figure 13a and S18). The larger amount of oxygen vacancies and defects on the ceria surface is inferred by Raman spectra as well as by CO chemisorption tests, where the intense peak at 2090 cm<sup>-1</sup> suggests an extensive presence of oxygen vacancies next to PdO(101) planes [62]. This is in accordance with the fact that the variety of Pd species present on 4PdAcCe(1173)M are likely to expose different Pd-PdO planes, including the undercoordinated

PdO(101) plane, which has been recently reported having a low methane activation energy [67,72,73]. Indeed, a thin PdO(101) layer on Pd [67,72,74], the presence of Pd at low temperature [75] or Pd<sup>4+</sup> ions on a mixed PdO<sub>x</sub> oxide [27] are conditions that have been recently indicated as extremely active for low temperature methane oxidation.

In addition, it is worth mentioning that these Pd species are well dispersed over the ceria surface, leaving less bare ceria on 4PdAcCe(1173)M compared to 4PdCe(1173)IW, as suggested by HRTEM and TPR analysis and further confirmed by XPS. The Pd/Ce atomic ratio estimated by XPS in the pretreated 4PdAcCe(1173)M sample is approximately 7 times greater than the ratio for 4PdCe(1173)IW. This is also illustrated in the Pd 3d region (Figure 12), as the data is plotted on an absolute scale. Nonetheless, the higher dispersion is not enough to explain the improved reaction rate (see Table 1), which is very likely due to the array of Pd<sup>0</sup>/Pd<sup>2+</sup> species stabilized via milling. DRIFTS “on-off” experiments further suggest that the reduced amount of free ceria surface might play a role in the lower deactivation rate observed during time-on-stream tests, as inactive side species appear to accumulate on bare ceria.

On the sample prepared by wet synthesis, the presence of higher PdO contribution is evidenced by XANES and EXAFS analysis, and larger PdO particles are detected by DRIFTS CO chemisorption tests, Raman spectroscopy and XRD analysis, including Rietveld refinement of the palladium peaks. Their large size also implies a highly crystalline structure, which is reflected in the sharper PdO peak at  $2\theta = 6.45^\circ$  in *in-situ* XRD diffractograms (Figure 8c) and in the stronger intensity of the Raman shift at  $646\text{ cm}^{-1}$  (Figure 9). Remarkably, the Pd 3d spectra highlight a superoxidized state of palladium on the IW sample, exhibiting mostly Pd<sup>4+</sup> and Pd<sup>2+</sup> species. As other bulk techniques (XAFS, XRD) show no trace of a crystalline PdO<sub>2</sub> structure, we believe that such superoxidized state is found at the surface of PdO particles, possibly as a PdO<sub>2</sub> overlayer. This would make it very different than what we reported in our previous paper [14], where we observed the coexistence of Pd<sup>2+</sup> and Pd<sup>4+</sup> on 1PdCeM after 1 (or 6) light-off cycle to 1173 K in a well-defined Pd-Ce amorphous shell structure. The higher Pd oxidation state may be also linked to the exposure at temperatures up to 1173 K; nevertheless, also according to the theoretical work by Senftle et al. [27], in order to achieve low methane activation barriers Pd<sup>4+</sup> moieties have to be found in a reactive Pd<sup>0</sup>/Pd<sup>2+</sup>/Pd<sup>4+</sup> environment, while AP-XPS spectra collected during reaction demonstrate a high stability of Pd<sup>4+</sup> species on the 4PdCe(1173)IW sample.

It is noteworthy that the morphology of 4PdOCe(1173)M, characterized by highly dispersed PdO nanoparticles, results in poor methane oxidation activity (see Figure S10). Our hypothesis is that supported PdO nanoparticles, either in weak interaction with ceria (as observed on PdO/CeO<sub>2</sub>

milled samples, both in this work and in our previous paper [14]) and/or in fully oxidized state (as those observed on IW) are not able to activate methane at low temperature. For this purpose, the heterogeneous mixture of Pd<sup>0</sup>/Pd<sup>2+</sup> species, likely arising from the strong interaction with ceria support and stabilized on its outermost layers, is needed, such as the one formed on 4PdAcCe(1173)M, where the nanoscale surface arrangement enables enhanced methane oxidation performance at low temperature and increased activity and stability at high temperatures. The intimate interaction of Ce<sup>3+</sup>/Ce<sup>4+</sup> and palladium ions in a stable arrangement maintained throughout reaction (Figure 11) likely promotes oxygen mobility and, consequently, a higher CH<sub>4</sub> oxidation rate and improved resistance against steam deactivation. On the other hand, dispersed PdO nanoparticles exhibiting mostly Pd<sup>4+</sup> and Pd<sup>2+</sup> species, as those observed on the sample prepared by incipient wetness impregnation and likely on the milled sample prepared using PdO nanoparticles, display poorer methane oxidation activity. The improved reactivity observed by *in-situ* DRIFTS under CH<sub>4</sub>-only atmosphere (Figure 13) further suggests that the Pd<sup>0</sup>/Pd<sup>2+</sup>/CeO<sub>x</sub> surface environment developed on 4PdAcCe(1173)M might provide enhanced performances also in other methane activation reactions, whereas Pd entities in an overoxidized state and in a highly crystalline form are less active for the activation of C-H bond and the low temperature oxidation of CH<sub>4</sub>.

## 5 Conclusions

Active methane oxidation catalysts were successfully prepared by dry mechano-chemical synthesis carried out using Pd(OAc)<sub>2</sub> and CeO<sub>2</sub> powders. PdAc/CeO<sub>2</sub> milled samples exhibited higher methane oxidation activity and stability compared to their counterparts prepared by traditional incipient wetness impregnation and by mechanical milling starting from Pd black, previously reported as the most active among evaluated materials [14]. Remarkably, the use of a palladium precursor salt also allowed for the successful loading of higher Pd content on low and high surface area ceria. Catalysts containing 4 wt% Pd displayed outstanding methane oxidation activity, outperforming the reference 4PdCeIW sample. Advanced *in-situ* and *ex-situ* characterization carried out on the 4PdAcCe(1173)M milled sample revealed a wide array of Pd species in a Pd<sup>0</sup>/Pd<sup>2+</sup> combination. These palladium species appear very stable, exhibiting small particle size (below 1.5 nm) and high dispersion. Conversely, on 4PdCe(1173)IW highly crystalline PdO particles are observed, predominantly comprised by Pd<sup>2+</sup> and Pd<sup>4+</sup>, leading to worse metal dispersion and a larger amount of free ceria surface. Such PdO/CeO<sub>2</sub> arrangement with more oxidized Pd species results in lower reactivity and a catalyst more prone to deactivation.

## **Acknowledgements**

MD acknowledges Regione Friuli Venezia Giulia for funding PhD under Operating Program of the European Social Fund 2014/2020. JL acknowledges funding by projects MICINN/FEDER RTI2018-093996-B-C31 and GC 2017 SGR 128. JL is a Serra Húnter Fellow and is grateful to the ICREA Academia program. NJD is grateful to Generalitat de Catalunya for fellowship grant 2018 BP 00146. The work carried out at Brookhaven National Laboratory was supported by the US Department of Energy under contract no. DE-SC0012704. S.D.S. is supported by a US Department of Energy Early Career Award. The XAS measurement used resources 7BM of the National Synchrotron Light Source II, a U.S. Department of Energy (DOE) Office of Science User Facility operated for the DOE Office of Science by Brookhaven National Laboratory under contract no. DE-SC0012704. The XRD experiments used resources of the Advanced Photon Source Beamline 17BM (XRD) at Argonne National Laboratory, which is an Office of Science User Facility operated for the U.S. Department of Energy (DOE) Office of Science and was supported by the U.S. DOE under contract no. DE-AC02-06CH11357.

## References

- [1] Z. Ma, X. Xiong, C. Song, B. Hu, W. Zhang, Electronic metal–support interactions enhance the ammonia synthesis activity over ruthenium supported on Zr-modified CeO<sub>2</sub> catalysts, *RSC Advances*. 6 (2016) 51106–51110. <https://doi.org/10.1039/C6RA10540H>.
- [2] W. Gao, Z.D. Hood, M. Chi, Interfaces in Heterogeneous Catalysts: Advancing Mechanistic Understanding through Atomic-Scale Measurements, *Accounts of Chemical Research*. 50 (2017) 787–795. <https://doi.org/10.1021/acs.accounts.6b00596>.
- [3] Y. Liu, Y. Ning, L. Yu, Z. Zhou, Q. Liu, Y. Zhang, H. Chen, J. Xiao, P. Liu, F. Yang, X. Bao, Structure and Electronic Properties of Interface-Confined Oxide Nanostructures, *ACS Nano*. 11 (2017) 11449–11458. <https://doi.org/10.1021/acsnano.7b06164>.
- [4] Y. Suchorski, S.M. Kozlov, I. Bespalov, M. Datler, D. Vogel, Z. Budinska, K.M. Neyman, G. Rupprechter, The role of metal/oxide interfaces for long-range metal particle activation during CO oxidation, *Nature Materials*. 17 (2018) 519–522. <https://doi.org/10.1038/s41563-018-0080-y>.
- [5] W. Huang, W.-X. Li, Surface and interface design for heterogeneous catalysis, *Phys. Chem. Chem. Phys.* 21 (2019) 523–536. <https://doi.org/10.1039/C8CP05717F>.
- [6] E. Aneggi, M. Boaro, S. Colussi, C. de Leitenburg, A. Trovarelli, Ceria-Based Materials in Catalysis: Historical Perspective and Future Trends, in: J.-C.G. Bünzli, V.K. Pecharsky (Eds.), *Handbook on the Physics and Chemistry of Rare Earths*, Elsevier, 2016: pp. 209–242. <https://doi.org/10.1016/bs.hpre.2016.05.002>.
- [7] K.-J. Zhu, J. Liu, Y.-J. Yang, Y.-X. Xu, B.-T. Teng, X.-D. Wen, M. Fan, A method to explore the quantitative interactions between metal and ceria for M/CeO<sub>2</sub> catalysts, *Surface Science*. 669 (2018) 79–86. <https://doi.org/10.1016/j.susc.2017.11.009>.
- [8] S. Colussi, A. Gayen, M. Farnesi Camellone, M. Boaro, J. Llorca, S. Fabris, A. Trovarelli, Nanofaceted Pd-O Sites in Pd-Ce Surface Superstructures: Enhanced Activity in Catalytic Combustion of Methane, *Angewandte Chemie International Edition*. 48 (2009) 8481–8484. <https://doi.org/10.1002/anie.200903581>.
- [9] M. Cargnello, J.J.D. Jaen, J.C.H. Garrido, K. Bakhtmutsky, T. Montini, J.J.C. Gamez, R.J. Gorte, P. Fornasiero, Exceptional Activity for Methane Combustion over Modular Pd@CeO<sub>2</sub> Subunits on Functionalized Al<sub>2</sub>O<sub>3</sub>, *Science*. 337 (2012) 713–717. <https://doi.org/10.1126/science.1222887>.
- [10] A. Gomathi, S.M. Vickers, R. Gholami, M. Alyani, R.W.Y. Man, M.J. MacLachlan, K.J. Smith, M.O. Wolf, Nanostructured Materials Prepared by Surface-Assisted Reduction: New Catalysts for Methane Oxidation, *ACS Applied Materials & Interfaces*. 7 (2015) 19268–19273. <https://doi.org/10.1021/acsami.5b05189>.
- [11] M. Hoffmann, S. Kreft, G. Georgi, G. Fulda, M.-M. Pohl, D. Seeburg, C. Berger-Karin, E.V. Kondratenko, S. Wohlrab, Improved catalytic methane combustion of Pd/CeO<sub>2</sub> catalysts via porous glass integration, *Applied Catalysis B: Environmental*. 179 (2015) 313–320. <https://doi.org/10.1016/j.apcatb.2015.05.028>.
- [12] T. Guo, J. Du, J. Wu, J. Li, Palladium catalyst supported on stair-like microstructural CeO<sub>2</sub> provides enhanced activity and stability for low-concentration methane oxidation, *Applied Catalysis A: General*. 524 (2016) 237–242. <https://doi.org/10.1016/j.apcata.2016.06.040>.
- [13] N. Wang, S. Li, Y. Zong, Q. Yao, Sintering inhibition of flame-made Pd/CeO<sub>2</sub> nanocatalyst for low-temperature methane combustion, *Journal of Aerosol Science*. 105 (2017) 64–72. <https://doi.org/10.1016/j.jaerosci.2016.11.017>.
- [14] M. Danielis, S. Colussi, C. de Leitenburg, L. Soler, J. Llorca, A. Trovarelli, Outstanding Methane Oxidation Performance of Palladium-Embedded Ceria Catalysts Prepared by a One-Step Dry Ball-Milling Method, *Angewandte Chemie International Edition*. 57 (2018) 10212–10216. <https://doi.org/10.1002/anie.201805929>.

- [15] M. Khader, M. Al-Marri, S. Ali, A. Abdelmoneim, Active and Stable Methane Oxidation Nano-Catalyst with Highly-Ionized Palladium Species Prepared by Solution Combustion Synthesis, *Catalysts*. 8 (2018) 66. <https://doi.org/10.3390/catal8020066>.
- [16] P. Lott, P. Dolcet, M. Casapu, J.-D. Grunwaldt, O. Deutschmann, The Effect of Prereduction on the Performance of Pd/Al<sub>2</sub>O<sub>3</sub> and Pd/CeO<sub>2</sub> Catalysts during Methane Oxidation, *Industrial & Engineering Chemistry Research*. 58 (2019) 12561–12570. <https://doi.org/10.1021/acs.iecr.9b01267>.
- [17] S. Colussi, P. Fornasiero, A. Trovarelli, Structure-activity relationship in Pd/CeO<sub>2</sub> methane oxidation catalysts, *Chinese Journal of Catalysis*. 41 (2020) 938–950. [https://doi.org/10.1016/S1872-2067\(19\)63510-2](https://doi.org/10.1016/S1872-2067(19)63510-2).
- [18] S. Roy, M.S. Hegde, Pd ion substituted CeO<sub>2</sub>: A superior de-NO<sub>x</sub> catalyst to Pt or Rh metal ion doped ceria, *Catalysis Communications*. 9 (2008) 811–815. <https://doi.org/10.1016/j.catcom.2007.09.019>.
- [19] M. Cargnello, T. Montini, S. Polizzi, N.L. Wieder, R.J. Gorte, M. Graziani, P. Fornasiero, Novel embedded Pd@CeO<sub>2</sub> catalysts: a way to active and stable catalysts, *Dalton Trans*. 39 (2010) 2122–2127. <https://doi.org/10.1039/B916035C>.
- [20] L.M. Misch, J.A. Kurzman, A.R. Derk, Y.-I. Kim, R. Seshadri, H. Metiu, E.W. McFarland, G.D. Stucky, C–H Bond Activation by Pd-substituted CeO<sub>2</sub>: Substituted Ions versus Reduced Species, *Chemistry of Materials*. 23 (2011) 5432–5439. <https://doi.org/10.1021/cm202709y>.
- [21] R.V. Gulyaev, A.I. Stadnichenko, E.M. Slavinskaya, A.S. Ivanova, S.V. Koscheev, A.I. Boronin, In situ preparation and investigation of Pd/CeO<sub>2</sub> catalysts for the low-temperature oxidation of CO, *Applied Catalysis A: General*. 439–440 (2012) 41–50. <https://doi.org/10.1016/j.apcata.2012.06.045>.
- [22] Z. Hu, X. Liu, D. Meng, Y. Guo, Y. Guo, G. Lu, Effect of Ceria Crystal Plane on the Physicochemical and Catalytic Properties of Pd/Ceria for CO and Propane Oxidation, *ACS Catalysis*. 6 (2016) 2265–2279. <https://doi.org/10.1021/acscatal.5b02617>.
- [23] G. Si, J. Yu, X. Xiao, X. Guo, H. Huang, D. Mao, G. Lu, Boundary role of Nano-Pd catalyst supported on ceria and the approach of promoting the boundary effect, *Molecular Catalysis*. 444 (2018) 1–9. <https://doi.org/10.1016/j.mcat.2017.10.025>.
- [24] A.D. Mayernick, M.J. Janik, Methane oxidation on Pd–Ceria: A DFT study of the mechanism over Pd<sub>x</sub>Ce<sub>1-x</sub>O<sub>2</sub>, Pd, and PdO, *Journal of Catalysis*. 278 (2011) 16–25. <https://doi.org/10.1016/j.jcat.2010.11.006>.
- [25] R.V. Gulyaev, T.Yu. Kardash, S.E. Malykhin, O.A. Stonkus, A.S. Ivanova, A.I. Boronin, The local structure of Pd<sub>x</sub>Ce<sub>1-x</sub>O<sub>2-xδ</sub> solid solutions, *Phys. Chem. Chem. Phys*. 16 (2014) 13523–13539. <https://doi.org/10.1039/C4CP01033G>.
- [26] T.P. Senftle, A.C.T. van Duin, M.J. Janik, Role of Site Stability in Methane Activation on Pd<sub>x</sub>Ce<sub>1-x</sub>O<sub>δ</sub> Surfaces, *ACS Catalysis*. 5 (2015) 6187–6199. <https://doi.org/10.1021/acscatal.5b00741>.
- [27] T.P. Senftle, A.C.T. van Duin, M.J. Janik, Methane Activation at the Pd/CeO<sub>2</sub> Interface, *ACS Catalysis*. 7 (2017) 327–332. <https://doi.org/10.1021/acscatal.6b02447>.
- [28] Y.-Q. Su, I.A.W. Filot, J.-X. Liu, Stable Pd-Doped Ceria Structures for CH<sub>4</sub> Activation and CO Oxidation, *ACS Catalysis*. 8 (2018) 75–80. <https://doi.org/10.1021/acscatal.7b03295>.
- [29] M. Danielis, S. Colussi, C. de Leitenburg, L. Soler, J. Llorca, A. Trovarelli, The effect of milling parameters on the mechanochemical synthesis of Pd–CeO<sub>2</sub> methane oxidation catalysts, *Catal. Sci. Technol*. 9 (2019) 4232–4238. <https://doi.org/10.1039/C9CY01098J>.
- [30] M. Danielis, S. Colussi, C. de Leitenburg, A. Trovarelli, The role of palladium salt precursors in Pd-PdO/CeO<sub>2</sub> catalysts prepared by dry milling for methane oxidation, *Catalysis Communications*. 135 (2020) 105899. <https://doi.org/10.1016/j.catcom.2019.105899>.
- [31] Y. Kamimura, M. Shimomura, A. Endo, Simple template-free synthesis of high surface area mesoporous ceria and its new use as a potential adsorbent for carbon dioxide capture, *Journal of Colloid and Interface Science*. 436 (2014) 52–62. <https://doi.org/10.1016/j.jcis.2014.08.047>.

- [32] N. Ohtake, Y. Yamane, K. Nakagawa, M. Katoh, S. Sugiyama, Hydrothermally Synthesized Ceria with a High Specific Surface Area for Catalytic Conversion of Ethanol to Ethylene, *Journal of Chemical Engineering of Japan*. 49 (2016) 197–203. <https://doi.org/10.1252/jcej.15we125>.
- [33] N. Ohtake, M. Katoh, S. Sugiyama, High thermal-stability ceria synthesized via thermal-hydrolysis route and methane-combustion performance, *Journal of the Ceramic Society of Japan*. 125 (2017) 57–61. <https://doi.org/10.2109/jcersj2.16255>.
- [34] M. Möller, N. Tarabanko, C. Wessel, R. Ellinghaus, H. Over, B.M. Smarsly, Electrospinning of CeO<sub>2</sub> nanoparticle dispersions into mesoporous fibers: on the interplay of stability and activity in the HCl oxidation reaction, *RSC Advances*. 8 (2018) 132–144. <https://doi.org/10.1039/C7RA03020G>.
- [35] Z. Feng, M. Zhang, Q. Ren, S. Mo, R. Peng, D. Yan, M. Fu, L. Chen, J. Wu, D. Ye, Design of 3-dimensionally self-assembled CeO<sub>2</sub> hierarchical nanosphere as high efficiency catalysts for toluene oxidation, *Chemical Engineering Journal*. 369 (2019) 18–25. <https://doi.org/10.1016/j.cej.2019.03.051>.
- [36] P.J. Chupas, K.W. Chapman, C. Kurtz, J.C. Hanson, P.L. Lee, C.P. Grey, A versatile sample-environment cell for non-ambient X-ray scattering experiments, *Journal of Applied Crystallography*. 41 (2008) 822–824. <https://doi.org/10.1107/S0021889808020165>.
- [37] B.H. Toby, R.B. Von Dreele, GSAS-II: the genesis of a modern open-source all purpose crystallography software package, *Journal of Applied Crystallography*. 46 (2013) 544–549. <https://doi.org/10.1107/S0021889813003531>.
- [38] B. Ravel, M. Newville, *ATHENA*, *ARTEMIS*, *HEPHAESTUS*: data analysis for X-ray absorption spectroscopy using *IFEFFIT*, *Journal of Synchrotron Radiation*. 12 (2005) 537–541. <https://doi.org/10.1107/S0909049505012719>.
- [39] R.M. Palomino, R. Hamlyn, Z. Liu, D.C. Grinter, I. Waluyo, J.A. Rodriguez, S.D. Senanayake, Interfaces in heterogeneous catalytic reactions: Ambient pressure XPS as a tool to unravel surface chemistry, *Journal of Electron Spectroscopy and Related Phenomena*. 221 (2017) 28–43. <https://doi.org/10.1016/j.elspec.2017.04.006>.
- [40] R.B. Anderson, Kinetics of Catalytic Reactions, in: R.B. Anderson (Ed.), *Experimental Methods in Catalytic Research*, Academic Press, 1968: pp. 1–43. <https://doi.org/10.1016/B978-0-12-058650-9.50006-2>.
- [41] J.J. Willis, A. Gallo, D. Sokaras, H. Aljama, S.H. Nowak, E.D. Goodman, L. Wu, C.J. Tassone, T.F. Jaramillo, F. Abild-Pedersen, M. Cargnello, Systematic Structure–Property Relationship Studies in Palladium-Catalyzed Methane Complete Combustion, *ACS Catalysis*. 7 (2017) 7810–7821. <https://doi.org/10.1021/acscatal.7b02414>.
- [42] A. Toso, S. Colussi, S. Padigapaty, C. de Leitenburg, A. Trovarelli, High stability and activity of solution combustion synthesized Pd-based catalysts for methane combustion in presence of water, *Applied Catalysis B: Environmental*. 230 (2018) 237–245. <https://doi.org/10.1016/j.apcatb.2018.02.049>.
- [43] V. Šepelák, S. Bégin-Colin, G. Le Caër, Transformations in oxides induced by high-energy ball-milling, *Dalton Transactions*. 41 (2012) 11927. <https://doi.org/10.1039/c2dt30349c>.
- [44] E. Furlani, E. Aneggi, C. de Leitenburg, S. Maschio, High energy ball milling of titania and titania–ceria powder mixtures, *Powder Technology*. 254 (2014) 591–596. <https://doi.org/10.1016/j.powtec.2014.01.075>.
- [45] H. Lieske, J. Voelter, Palladium redispersion by spreading of palladium(II) oxide in oxygen treated palladium/alumina, *The Journal of Physical Chemistry*. 89 (1985) 1841–1842. <https://doi.org/10.1021/j100256a001>.
- [46] G. Chen, W.-T. Chou, C. Yeh, The sorption of hydrogen on palladium in a flow system, *Applied Catalysis*. 8 (1983) 389–397. [https://doi.org/10.1016/0166-9834\(83\)85009-X](https://doi.org/10.1016/0166-9834(83)85009-X).

- [47] S. Lin, L. Yang, X. Yang, R. Zhou, Redox behavior of active PdO<sub>x</sub> species on (Ce,Zr)<sub>x</sub>O<sub>2</sub>-Al<sub>2</sub>O<sub>3</sub> mixed oxides and its influence on the three-way catalytic performance, *Chemical Engineering Journal*. 247 (2014) 42–49. <https://doi.org/10.1016/j.cej.2014.03.015>.
- [48] Y. Cao, R. Ran, X. Wu, B. Zhao, J. Wan, D. Weng, Comparative study of ageing condition effects on Pd/Ce<sub>0.5</sub>Zr<sub>0.5</sub>O<sub>2</sub> and Pd/Al<sub>2</sub>O<sub>3</sub> catalysts: Catalytic activity, palladium nanoparticle structure and Pd-support interaction, *Applied Catalysis A: General*. 457 (2013) 52–61. <https://doi.org/10.1016/j.apcata.2013.03.002>.
- [49] M.-F. Luo, X.-M. Zheng, Redox behaviour and catalytic properties of Ce<sub>0.5</sub>Zr<sub>0.5</sub>O<sub>2</sub>-supported palladium catalysts, *Applied Catalysis A: General*. 189 (1999) 15–21. [https://doi.org/10.1016/S0926-860X\(99\)00230-6](https://doi.org/10.1016/S0926-860X(99)00230-6).
- [50] V. Ferrer, A. Moronta, J. Sánchez, R. Solano, S. Bernal, D. Finol, Effect of the reduction temperature on the catalytic activity of Pd-supported catalysts, *Catalysis Today*. 107–108 (2005) 487–492. <https://doi.org/10.1016/j.cattod.2005.07.059>.
- [51] Y. Xu, F. Wang, X. Liu, Y. Liu, M. Luo, B. Teng, M. Fan, X. Liu, Resolving a Decade-Long Question of Oxygen Defects in Raman Spectra of Ceria-Based Catalysts at Atomic Level, *The Journal of Physical Chemistry C*. 123 (2019) 18889–18894. <https://doi.org/10.1021/acs.jpcc.9b00633>.
- [52] J.R. McBride, K.C. Hass, W.H. Weber, Resonance-Raman and lattice-dynamics studies of single-crystal PdO, *Physical Review B*. 44 (1991) 5016–5028. <https://doi.org/10.1103/PhysRevB.44.5016>.
- [53] C. Li, Y. Sakata, T. Arai, K. Domen, K. Maruya, T. Onishi, Carbon monoxide and carbon dioxide adsorption on cerium oxide studied by Fourier-transform infrared spectroscopy. Part 1.—Formation of carbonate species on dehydroxylated CeO<sub>2</sub>, at room temperature, *Journal of the Chemical Society, Faraday Transactions 1: Physical Chemistry in Condensed Phases*. 85 (1989) 929. <https://doi.org/10.1039/f19898500929>.
- [54] O. Demoulin, M. Navez, P. Ruiz, Investigation of the behaviour of a Pd/γ-Al<sub>2</sub>O<sub>3</sub> catalyst during methane combustion reaction using in situ DRIFT spectroscopy, *Applied Catalysis A: General*. 295 (2005) 59–70. <https://doi.org/10.1016/j.apcata.2005.08.008>.
- [55] Z. Li, G. Xu, G.B. Hoflund, In situ IR studies on the mechanism of methane oxidation over Pd/Al<sub>2</sub>O<sub>3</sub> and Pd/Co<sub>3</sub>O<sub>4</sub> catalysts, *Fuel Processing Technology*. 84 (2003) 1–11. [https://doi.org/10.1016/S0378-3820\(02\)00099-1](https://doi.org/10.1016/S0378-3820(02)00099-1).
- [56] K. Khivantsev, N.R. Jaegers, I.Z. Koleva, H.A. Aleksandrov, L. Kovarik, M. Engelhard, F. Gao, Y. Wang, G.N. Vayssilov, J. Szanyi, Stabilization of Super Electrophilic Pd<sup>+2</sup> Cations in Small-Pore SSZ-13 Zeolite, *J. Phys. Chem. C*. 124 (2020) 309–321. <https://doi.org/10.1021/acs.jpcc.9b06760>.
- [57] I. Jbir, J. Couble, S. Khaddar-Zine, Z. Ksibi, F. Meunier, D. Bianchi, Individual Heat of Adsorption of Adsorbed CO Species on Palladium and Pd–Sn Nanoparticles Supported on Al<sub>2</sub>O<sub>3</sub> by Using Temperature-Programmed Adsorption Equilibrium Methods, *ACS Catalysis*. 6 (2016) 2545–2558. <https://doi.org/10.1021/acscatal.5b02749>.
- [58] J.F. Weaver, J. Choi, V. Mehar, C. Wu, Kinetic Coupling among Metal and Oxide Phases during CO Oxidation on Partially Reduced PdO(101): Influence of Gas-Phase Composition, *ACS Catalysis*. 7 (2017) 7319–7331. <https://doi.org/10.1021/acscatal.7b02570>.
- [59] N.M. Martin, M. Van den Bossche, H. Grönbeck, C. Hakanoglu, F. Zhang, T. Li, J. Gustafson, J.F. Weaver, E. Lundgren, CO Adsorption on Clean and Oxidized Pd(111), *The Journal of Physical Chemistry C*. 118 (2014) 1118–1128. <https://doi.org/10.1021/jp410895c>.
- [60] H. Stotz, L. Maier, A. Boubnov, A.T. Gremminger, J.-D. Grunwaldt, O. Deutschmann, Surface reaction kinetics of methane oxidation over PdO, *Journal of Catalysis*. 370 (2019) 152–175. <https://doi.org/10.1016/j.jcat.2018.12.007>.
- [61] Z. Liu, F. Zhang, N. Rui, X. Li, L. Lin, L.E. Betancourt, D. Su, W. Xu, J. Cen, K. Attenkofer, H. Idriss, J.A. Rodriguez, S.D. Senanayake, Highly Active Ceria-Supported Ru Catalyst for

- the Dry Reforming of Methane: In Situ Identification of Ru<sup>δ+</sup>-Ce<sup>3+</sup> Interactions for Enhanced Conversion, *ACS Catalysis*. 9 (2019) 3349–3359. <https://doi.org/10.1021/acscatal.8b05162>.
- [62] J.F. Weaver, F. Zhang, L. Pan, T. Li, A. Asthagiri, Vacancy-Mediated Processes in the Oxidation of CO on PdO(101), *Accounts of Chemical Research*. 48 (2015) 1515–1523. <https://doi.org/10.1021/acs.accounts.5b00101>.
- [63] A. Bensalem, J.-C. Muller, D. Tessier, F. Bozon-Verduraz, Spectroscopic study of CO adsorption on palladium-ceria catalysts, *J. Chem. Soc.. Faraday Trans.* 92 (1996) 3233–3237. <https://doi.org/10.1039/FT9969203233>.
- [64] S. Colussi, A. Trovarelli, G. Groppi, J. Llorca, The effect of CeO<sub>2</sub> on the dynamics of Pd–PdO transformation over Pd/Al<sub>2</sub>O<sub>3</sub> combustion catalysts, *Catalysis Communications*. 8 (2007) 1263–1266. <https://doi.org/10.1016/j.catcom.2006.11.020>.
- [65] H. Peng, C. Rao, N. Zhang, X. Wang, W. Liu, W. Mao, L. Han, P. Zhang, S. Dai, Confined Ultrathin Pd-Ce Nanowires with Outstanding Moisture and SO<sub>2</sub> Tolerance in Methane Combustion, *Angewandte Chemie International Edition*. 57 (2018) 8953–8957. <https://doi.org/10.1002/anie.201803393>.
- [66] H. Duan, R. You, S. Xu, Z. Li, K. Qian, T. Cao, W. Huang, X. Bao, Pentacoordinated Al<sup>3+</sup>-Stabilized Active Pd Structures on Al<sub>2</sub>O<sub>3</sub>-Coated Palladium Catalysts for Methane Combustion, *Angewandte Chemie International Edition*. 58 (2019) 12043–12048. <https://doi.org/10.1002/anie.201904883>.
- [67] N.M. Kinnunen, J.T. Hirvi, M. Suvanto, T.A. Pakkanen, Role of the Interface between Pd and PdO in Methane Dissociation, *The Journal of Physical Chemistry C*. 115 (2011) 19197–19202. <https://doi.org/10.1021/jp204360c>.
- [68] A. Trincherro, A. Hellman, H. Grönbeck, Metal-oxide sites for facile methane dissociation: Metal-oxide sites for facile methane dissociation, *Physica Status Solidi (RRL) - Rapid Research Letters*. 8 (2014) 605–609. <https://doi.org/10.1002/pssr.201409090>.
- [69] Y.-Q. Su, J.-X. Liu, I.A.W. Filot, L. Zhang, E.J.M. Hensen, Highly Active and Stable CH<sub>4</sub> Oxidation by Substitution of Ce<sup>4+</sup> by Two Pd<sup>2+</sup> Ions in CeO<sub>2</sub> (111), *ACS Catalysis*. 8 (2018) 6552–6559. <https://doi.org/10.1021/acscatal.8b01477>.
- [70] S. Colussi, A. Trovarelli, E. Vesselli, A. Baraldi, G. Comelli, G. Groppi, J. Llorca, Structure and morphology of Pd/Al<sub>2</sub>O<sub>3</sub> and Pd/CeO<sub>2</sub>/Al<sub>2</sub>O<sub>3</sub> combustion catalysts in Pd–PdO transformation hysteresis, *Applied Catalysis A: General*. 390 (2010) 1–10. <https://doi.org/10.1016/j.apcata.2010.09.033>.
- [71] M.H. Enayati, F.A. Mohamed, Application of mechanical alloying/milling for synthesis of nanocrystalline and amorphous materials, *International Materials Reviews*. 59 (2014) 394–416. <https://doi.org/10.1179/1743280414Y.0000000036>.
- [72] A. Hellman, A. Resta, N.M. Martin, J. Gustafson, A. Trincherro, P.-A. Carlsson, O. Balmes, R. Felici, R. van Rijn, J.W.M. Frenken, J.N. Andersen, E. Lundgren, H. Grönbeck, The Active Phase of Palladium during Methane Oxidation, *J. Phys. Chem. Lett.* 3 (2012) 678–682. <https://doi.org/10.1021/jz300069s>.
- [73] Y.-H. (Cathy) Chin, C. Buda, M. Neurock, E. Iglesia, Consequences of Metal–Oxide Interconversion for C–H Bond Activation during CH<sub>4</sub> Reactions on Pd Catalysts, *Journal of the American Chemical Society*. 135 (2013) 15425–15442. <https://doi.org/10.1021/ja405004m>.
- [74] N.M. Martin, M. Van den Bossche, A. Hellman, H. Grönbeck, C. Hakanoglu, J. Gustafson, S. Blomberg, N. Johansson, Z. Liu, S. Axnanda, J.F. Weaver, E. Lundgren, Intrinsic Ligand Effect Governing the Catalytic Activity of Pd Oxide Thin Films, *ACS Catalysis*. 4 (2014) 3330–3334. <https://doi.org/10.1021/cs5010163>.
- [75] D. Wang, J. Gong, J. Luo, J. Li, K. Kamasamudram, N. Currier, A. Yezerets, Distinct reaction pathways of methane oxidation on different oxidation states over Pd-based three-way catalyst (TWC), *Applied Catalysis A: General*. 572 (2019) 44–50. <https://doi.org/10.1016/j.apcata.2018.12.022>.